Evaluation of computational and physical parameters influencing CFD simulations of pollutant dispersion in building arrays

Yuwei Dai[a], Cheuk Ming Mak[a] *, Zhengtao Ai[b], Jian Hang[c]

[a] Department of Building Services Engineering, The Hong Kong Polytechnic University, Hong Kong, China

[b] International Center for Indoor Environment and Energy, Department of Civil Engineering, Technical University of Denmark

[c] Department of Atmospheric Science, School of Environmental Science and Engineering, Sun Yat-Sen University

*Corresponding author: Cheuk Ming Mak, Department of Building Services Engineering, The Hong Kong Polytechnic University, Hung Hom, Kowloon, Hong Kong. Email: cheuk-ming.mak@polyu.edu.hk

Abstract

Many CFD studies have investigated the influence of computational parameters on the predicted concentration distribution of pollutants around isolated buildings, but such studies for building arrays are still lacking. This study systematically evaluated the influence of four computational and two physical parameters on pollutant dispersion in building arrays, including turbulence models, grid resolution, discretization of time step size Δt, length of sampling period, aspect ratio of the arrays, and release rate of tracer gas. Throughout these evaluations, a set of published wind tunnel experimental data was used to validate the CFD models. For concentration simulations, the Large Eddy Simulation (LES) model gave the most accurate results but still had limitations in areas near the source, whereas the Detached Eddy Simulation (DES) and the Reynolds Averaged Navier-Strokes (RANS) RNG $k - \varepsilon$ models underperformed in some areas. The results of the LES and DES simulations varied with changes in Δt^* and sampling length until Δt^* was less than 0.24 and the sampling length was higher than $2400\Delta t^*$ for LES and $1200\Delta t^*$ for DES. A larger aspect ratio did not necessarily result in a higher concentration field than a smaller ratio. An increase in the tracer gas release rate did not change the general dispersion characteristics, but it still affected the concentration distribution in the areas near the source and resulted in a larger polluted area. The findings of this study are intended to contribute to improvements in the quality of CFD simulations of pollutant dispersion in building arrays.

Keywords: CFD simulation, pollutant dispersion, building arrays, computational parameters, sensitivity test.

Greek symbols

Δ	grid scale
ε	turbulent viscous dissipation rate (m^2/s^3)
η_0	model constant
κ	Von Karman constant, 0.4187
μ_t	subgrid-scale turbulent viscosity(m^2/s)
ϑ	turbulent viscosity (m^2/s)
ξ	model constant
ρ	air density (Kg/m^3)
τ_{ij}	subgrid-scale (SGS) stresses

Nomenclature

C_1	empirical constant, 0.025
C_2	empirical constant, 0.41
C_{des}	empirical constant, 0.65
C_S	Smagorinsky constant, 0.1
C_μ	model constant, 0.069
C_{local}	measured concentration (ppm)
C_{source}	source concentration (ppm)
d	length scale
H	building height, $0.125 m$
k	turbulent kinetic energy (m^2/s^2)
K_c	non-dimensional concentration
u_i	air velocity (m/s)
p	pressure (Pa)
Q_{source}	flow rate of the source emission (m^3/s)
Sc_t	turbulent Schmidt number
Sc_{SGS}	turbulent Schmidt number for SGS motions
S_{ij}	strain rate tensor
Δt	time step size (s)
Δt^*	non-dimensional time step size
u_i	velocity component
U	wind velocity (m/s)
U^*	non-dimensional velocity component
U_{ref}	reference wind speed (m/s)
V^*	non-dimensional velocity component
y^+	dimensionless wall distance
z_0	roughness height, $0.00075 m$

1. Introduction

Air pollutant dispersion near and around buildings is an essential environmental issue with respect to human health. In an urban environment, various sources of air pollution, including traffic exhaust, dust, pollen, airborne viruses, and toxic and odorous emissions [1], may have harmful consequences. Air quality is one of the most important problems in urban areas, so the evaluation of pollutant dispersion is of great interest. However, the distribution of contaminants depends greatly upon the complex interactions between atmospheric flow and flow around obstacles. Therefore, precise prediction of pollutant dispersion is difficult due to the complicated flow structure perturbed by building obstacles.

In recent decades, many studies have investigated air pollution aerodynamics with multiple methods, ranging from semi-empirical methods, field tests, and wind tunnel experiments to Computational Fluid Dynamics (CFD). The use of Semi-empirical models like Gaussian model [2] and so-called ASHRAE models [3, 4] to estimate contaminant dispersion is relatively simple, but at the expense of abundant uncertainty and limited applicability. Some field tests have been performed to reveal the transport process under real atmospheric situations [5-12]. These full-scale measurements consider all phenomena to collect data on the real complexity of the airflow and dispersion fields. However, full-scale experiments are measured at a limited number of positions in the field under uncontrolled wind and weather conditions that are impossible to repeat. Wind tunnel experimentation is regarded as a useful approach with controllable boundary conditions to predict and analyze contaminant dispersion [13-21], but it still suffers from a limited number of test points and from similarity requirements. Furthermore, both field tests and wind tunnel experiments are expensive and time-consuming.

Numerical simulations with CFD [22-24] show some advantages over other methods and have become an alternative tool to investigate pollutant dispersion around buildings that can provide complete field

data with no limitation of similarity requirements. Studies have shown that CFD methods can accurately reproduce airflow and pollutant dispersion fields [25] and are especially suitable for parametric studies of various boundary conditions and dispersion processes [26]. Some recent reviews have summarized the current CFD modeling issues and the key features of near-field pollutant dispersion in urban environments [27-29]. For CFD prediction, the choices of appropriate numerical settings, including physical geometry, computational domain dimensions, turbulence models, grid resolutions, boundary conditions, solution methods, and iterative convergence, are fundamental to ensure accuracy and reliability. Among others, turbulence models strongly determine the predictive accuracy of pollutant dispersion, considering the inherent unsteadiness of the flow field around buildings. Turbulence models are generally categorized into two families: steady models, such as Reynolds-averaged Navier-Strokes (RANS), and transient models, such as Large Eddy Simulation (LES).

Steady-state RANS models are widely used to predict pollutant dispersion in urban aerodynamics because of their relatively short computing times and lower hardware costs. Several studies have compared various RANS models [16, 30-33] and reported that the RNG $k - \varepsilon$ model [34, 35] predicts flow and concentration fields better than other $k - \varepsilon$ models [36], including the Standard $k - \varepsilon$ model [37]. Other studies [33, 38] have indicated that when the turbulence produced by neighboring buildings is predominant, the differences among various RANS models for concentration diffusion are unimportant in street canyons or building complexes. Several studies [39, 40] investigated the air pollutant dispersion mechanism in high density building arrays with RANS model (RNG $k - \varepsilon$ and SST $k - \omega$ model), but they mainly focused on the general transportation routes and mean flows in building arrays and canyons. Because of the Reynolds-averaged treatments, the RANS models have some difficulties in predicting the accurate airflow and concentration fields around buildings; for example, they may overestimate the turbulent kinetic energy on the windward wall of a building [41] or over-predict the reattachment lengths on the roof and behind the building [42].

The LES model predicts flow and concentration fields more accurately than RANS models, but it carries a higher cost of computational resources. Some earlier studies compared the performance of RANS and LES models based on urban aerodynamics and pollutant dispersion around buildings [26, 43-47]; they concluded that the LES model predicts the mean distribution of concentrations better than RANS models, although the discrepancy in the mean velocity fields given by these two models is relatively small. The LES model can reproduce well the anisotropic concentration diffusions that inherently fluctuate, which cannot be reproduced by RANS models. Shi et al. [48] compared the flow and concentration fields produced by LES model and by a wind tunnel experiment with staggered building arrays and revealed that such complicated flow fields should be considered in application of LES model. Furthermore, the treatment of boundary conditions is more complex in LES modeling than in RANS models, and many factors are likely to influence the quality of LES simulation. Lau and Ngan [49] compared the air velocity predicted by LES model and RANS model in building arrays. They found that the LES results were better than RANS results, which suggested that in building arrays, the flow was highly fluctuated and not suitable for the homogeneous emission method. However, the comparison of the simulated pollutant concentration was not included in their study. Ai and Mak [50] analyzed various influencing parameters regarding LES modeling of flow and dispersion around an isolated building and conducted sensitivity analyses of several factors. However, the significant interactions among building groups contain much more convoluted fluctuating flows and concentration fields than an isolated building. Therefore, a detailed evaluation of the influencing parameters of LES models regarding pollutant dispersion in building arrays is needed. In addition, no detailed comparison in the prediction of pollutant dispersion of the performance of RANS and LES models in building arrays has been performed.

More recently, a hybrid unsteady RANS/LES model, known as detached-eddy simulation (DES) model [51], has been adopted to study the wind field around building blocks. Some studies compared the results of DES models and RANS models, including steady and unsteady RANS models, and revealed

that DES model better captures the key feature of mean flow fields than RANS models as compared with the data from wind tunnel experiments [52-54]. Liu and Niu [55] evaluated the performances of RANS, LES, and DES models in predicting wind flow around an isolated building via analysis of several computational parameters. They revealed that the DES model could predict similar results for the mean airflow field on the leeward side of the building and fluctuating characteristics with the LES model but required fewer numerical resources. However, only a few studies have adopted DES model to investigate the pollutant dispersion problem. Kakosimos and Assael [53] simulated the gas dispersion released in building arrays with the DES model. They indicated that the flow pattern and concentration both agreed well with the experiment datasets and suggested that the DES model is a viable alternative to the LES and RANS models. However, Lateb et al. [54] presented a two-building case of flow and dispersion fields of a pollutant emitted from a rooftop stack and indicated that the DES model predicted better wind flow fields but similar average errors in terms of concentration fields than the RANS model (RNG $k - \varepsilon$). The paradox between former studies reveals the need for a detailed evaluation of the DES model in the pollutant dispersion problem. The effects of some factors on the DES results for the pollutant dispersion in building arrays are still unclear, as well as the differences from the results of the RANS and LES models.

The effects of computational parameters on the DES and LES simulations of pollutant dispersion in building arrays have yet to be comprehensively evaluated. These parameters include the mesh resolution and the discretization of the time step size and the sampling length to obtain a time-averaged field. In addition to the aforementioned computational parameters, two physical parameters—the aspect ratio (AR; building height to street width) and the release rate of tracer gas—are also important in studies of pollutant dispersion in building arrays and thus require examination. The objective of this study is therefore to evaluate the performances of steady RANS, LES and DDES (Delayed Detached Eddy Simulation) model, with different computational settings, to suggest appropriate selections from the view of both predictive accuracy and numerical costs, and to examine the two physical factors with the suggested computational settings based on a published wind tunnel experiment model [56]. The findings of this study are intended to provide information and suggestions for future CFD simulations to acquire more accurate pollutant modelling in complex built environment. Further, it can also help researcher to design wind tunnel tests, even field tests, of flow and concentrations. Section 2 introduces the theories of the three turbulence models, and the wind tunnel experiment is elaborated in Section 3. Section 4 presents the computational settings of the numerical simulations, and the sensitivity analysis and discussions of computational parameters of the CFD simulation are presented in Section 5. Further investigations of different ARs and release rates of tracer gas are demonstrated in Section 6, and Section 7 summarizes and concludes the paper.

2. CFD methods

2.1 RANS and LES models

The governing equations in both RANS and LES models for incompressible Newtonian fluids can be written as follows:

$$\frac{\partial \overline{u_i}}{\partial x_i} = 0, \tag{1}$$

$$\frac{\partial(\rho \overline{u_i})}{\partial t} + \frac{\partial(\rho \overline{u_i u_j})}{\partial x_j} = -\frac{\partial \overline{p}}{\partial x_i} + \vartheta \frac{\partial^2 \overline{u_i}}{\partial x_i^2} - \frac{\partial \tau_{ij}}{\partial x_j}, \tag{2}$$

$$\frac{\partial(\rho \overline{c})}{\partial t} + \frac{\partial(\rho \overline{u_j c})}{\partial x_j} = -\frac{\partial J_j}{\partial x_j}, \tag{3}$$

where u_i and u_j are velocity components, p is the pressure, ρ represents density, and ϑ is viscosity.

For RANS models, the overbar ($\overline{}$) indicates time-averaged components. In this study, only the RNG $k - \varepsilon$ model is adopted, which shows a number of improvements over the standard $k - \varepsilon$ model. An additional strain-dependent term, R_ε, in the transport equation for ε gives the RNG model greater sensitivity in dealing with rapid strain and streamline curvature than the standard $k - \varepsilon$ model. The added term R_ε is shown by the equation as:

$$R_\varepsilon = \frac{C_\mu \rho \eta^3 (1 - \eta/\eta_0)}{1 + \xi \eta^3} \cdot \frac{\varepsilon^2}{k} \tag{4}$$

where C_μ, η_0, and ξ are model constants, and $\eta \equiv Sk/\varepsilon$ where S is the scale of strain rate.

For the LES model, the overbars ($\overline{}$) represent filtered variables. In the filtering operation, the terms τ_{ij} and J_j are contained in the momentum equation and the concentration equation, which are usually termed as subgrid-scale (SGS) stresses, defined as:

$$\tau_{ij} = \rho \overline{u_i u_j} - \rho \overline{u_i}\, \overline{u_j}, \tag{5}$$

$$J_j = \overline{u_j c} - \overline{u_j}\, \overline{c}, \tag{6}$$

The Boussinesq hypothesis [57] is used to correlate the term τ_{ij} with strain rate tensor $\overline{S_{ij}}$ to close the governing equation, which are defined by:

$$\tau_{ij} - \frac{1}{3} \tau_{kk} \sigma_{ij} = -2\mu_t \overline{S}_{ij}, \tag{7}$$

$$\overline{S_{ij}} = \frac{1}{2} \left(\frac{\partial \overline{u_i}}{\partial x_j} + \frac{\partial \overline{u_j}}{\partial x_i} \right), \tag{8}$$

where μ_t is the subgrid-scale turbulent viscosity, and the isotropic part τ_{kk} is zero for incompressible flows. In this study, μ_t is modeled by the Smagorinsky–Lilly model [58, 59] and is calculated by:

$$\mu_t = (C_S \Delta)^2 \sqrt{2 \overline{S}_{ij} \overline{S}_{ij}}, \tag{9}$$

where the Smagorinsky constant C_S is empirically given as 0.1, and Δ is the grid scale.

2.2 DES model

In the DES model, which combines the RANS and LES models, the unsteady RANS is used in the boundary layer and the LES is used for the separate flow regions. A new length scale, $\tilde{d} = \min(d, C_{des}\Delta)$, is defined in the standard Spalart-Allmaras DES model [51], where Δ represents the largest grid scale in the x, y, or z directions of the grid cell ($\Delta = \max(\Delta x, \Delta y, \Delta z)$) and the empirical value C_{des} equals 0.65 for the adjustable scalar on structured meshes. In the DES model, the LES mode is used if $\Delta \ll d$, and the unsteady RANS mode is used if $\Delta \gg d$. The newly defined length scale $\tilde{d}$ would guarantee the needed model as switching over between the LES and RANS modes.

Furthermore, Spalart et al. [51, 60] revised the standard DES model into the delayed DES model, which preserved the RANS model in the boundary layer to improve the accuracy of simulations near the wall region. Based upon the discussions and recommendations from previous studies [52, 60], the Delayed DES model (DDES) is adopted in this study.

3. Description of the wind tunnel experiment

A wind tunnel experiment conducted at the University of Hamburg [56] measured the airflow and dispersions in a finite array of rectangular building models (CEDVAL B1-1) in the Blasius wind tunnel. The building model was at a reduced scale of 1:200. The experimental model consisted of a 3×7 array of buildings, and one target building had four facing pollutant sources located on the leeward wall, as

shown in Fig. 1. The boundary layer flow in the experiment was validated by full-scale data in the test section before the building model was constructed. The airflow and concentration fields were measured by Laser Droppler Velocimetry (LVD) technique and Flame Ionization Detector (FID), respectively. Test points were measured on five planes: four vertical planes at $Y = -H, Y = -0.6H, Y = -0.4H$, and $Y = 0$, and a horizontal plane at $Z = 0.5H$. The tracer gas (CO_2) was uniformly released from the four sources with a constant velocity of $0.025m/s$. Emission data were acquired within one horizontal measurement plane at $Z = 1.5m$ (full scale) height. The Reynolds number was 37,252 based on the reference velocity of $6\ m/s$ at the building height ($H = 0.125m$). The average exhaust velocity of the pollutant source was $0.025\ m/s$. The turbulence kinetic energy k was determined by the measured fluctuating velocities, $k = 0.5(u^{´2} + v^{´2} + w^{´2})$. The concentration value was obtained in a non-dimensional form as [53]:

$$K_c = \frac{C_{local}}{C_{source}} \cdot \frac{U_{ref}H^2}{Q_{source}} \tag{10}$$

where C_{local} was the measured concentration (ppm) with the environmental background concentration subtracted, C_{source} was the concentration (ppm) at the source, U_{ref} was the reference wind speed (m/s) measured at $0.66m$, H was the building height ($H = 0.125m$), and Q_{source} was the flow rate of the source emission (m^3/s).
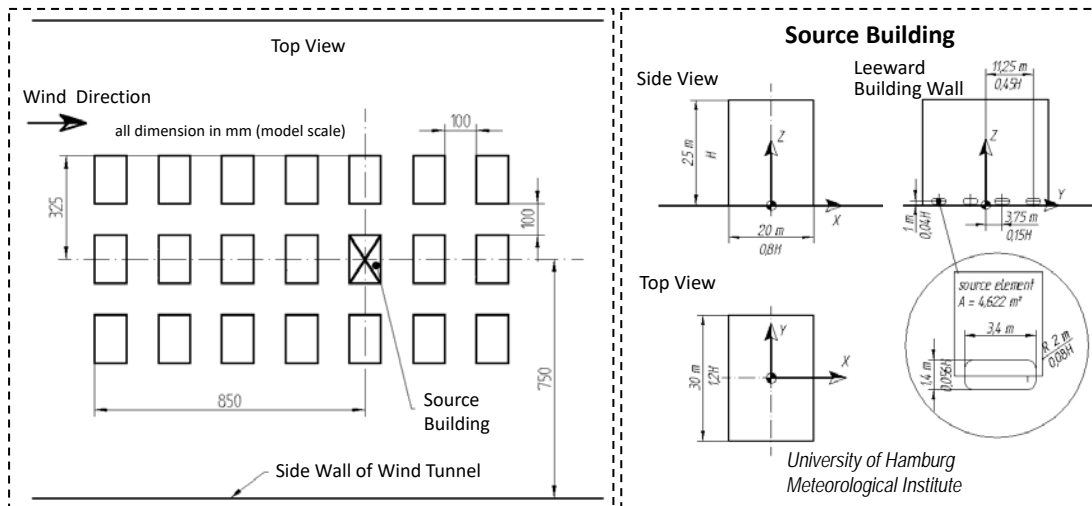

Fig. 1. Dimensions of the building models, the source building, and the source [56].

4. Computational settings

4.1 Computational domain and grid generation

The computational domain size was length ×width ×height $= 33H \times 12H \times 6H$, as shown in Fig. 2, which was based on the best-practice guidelines [61], except for the lateral distance. The lateral distance was based upon the wind tunnel width to ensure an accurate reproduction. The blockage ratio of the domain size was 1.67%, which was lower than the recommended criteria (3%) [61].
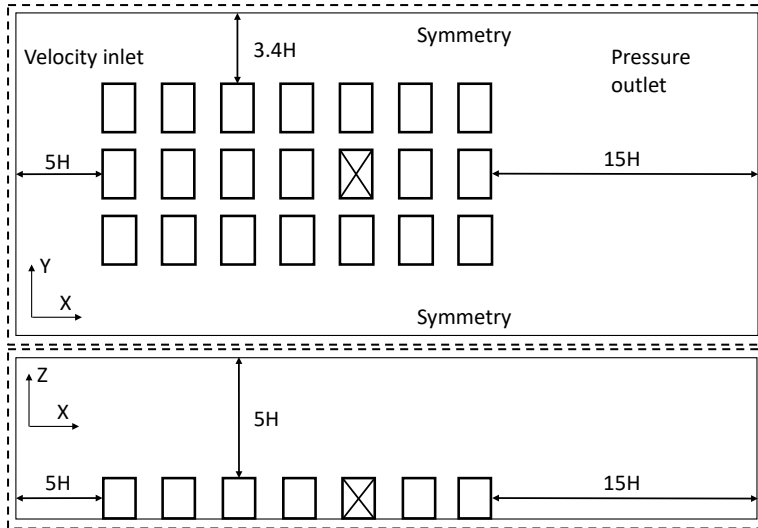
Fig. 2. Computational domain: top view and side view.

Three mesh systems were constructed with coarse, medium, and fine structured hexahedral grids, with minimum cell widths of 0.001, 0.0005, and 0.00025m, respectively. The total numbers of meshes were approximately 3.2 million, 5.9 million, and 9.4 million, respectively. Information on grid construction is given in Fig. 3.
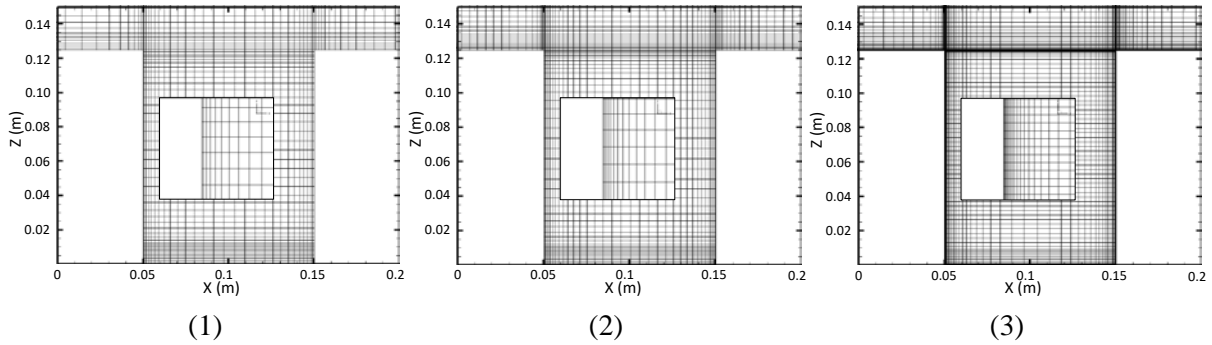

Fig. 3. Mesh resolution of three systems: (1) minimum grid size, 0.001m; (2) minimum grid size, 0.0005m; (3) minimum grid size, 0.00025m.

4.2 Boundary conditions

The inlet boundary conditions of the domain followed a logarithm way and are presented by the profiles of mean wind velocity U, turbulent kinetic energy k, and turbulent dissipation rate ε, as summarized in Table 1. The coefficients in Table 1 were determined by fitting them with experiment data, which were $z_0 = 0.00075m$, $u^* = 0.4078m/s$, $C_1 = 0.025$ and $C_2 = 0.41$. In addition, the Von Karman constant κ is 0.4187 and $C_\mu = 0.069$. Based on the predefined k and ε, the vertex method with 190 vortices was adopted to randomly generate the fluctuations in the mean velocity profile at the inlet plane. Some studies adopted vortex method in the LES or DES simulations which provided good results of the wind flow fields and concentration fields around an isolated building, such as Ai et al.[50] and Liu et al.[52]. The two layer models were adopted for RNG $k - \varepsilon$ simulations to the near-wall treatment because they showed better performance than the standard wall functions [35, 62]. The near-wall area was resolved by the enhanced wall functions directly on the condition that the y^+ of the first near-wall mesh was less than 5.

To simulate the pollutant dispersion, the tracer gas (CO_2) was uniformly released from the four source elements with a constant velocity of $0.025m/s$ in the X direction. No perturbations were considered for the emissions of pollutants. When the concentration equation was solved, the turbulent Schmidt

number Sc_t of 0.7 was adopted for the RANS model, whereas that for SGS motions (Sc_{SGS}) of 0.4 was used for the LES and DES models.

Table 1. Boundary conditions.

	Power law type
Domain inlet	$U = \dfrac{u^*}{\kappa} \ln\left(\dfrac{z + z_0}{z_0}\right)$
	$k = \sqrt{C_1 \cdot \ln(z + z_0) + C_2}$
	$\varepsilon = \dfrac{u^* \sqrt{C_\mu}}{\kappa(z + z_0)} \sqrt{C_1 \cdot \ln(z + z_0) + C_2}$
Domain outlet	$\dfrac{\partial}{\partial x}(u, v, w, k, \varepsilon) = 0$
Domain celling	$w = 0, \dfrac{\partial}{\partial x}(u, v, k, \varepsilon) = 0$
Domain lateral sides	$v = 0, \dfrac{\partial}{\partial x}(u, w, k, \varepsilon) = 0$
Domain ground	Enhanced wall functions
Building surfaces	Non-slip for wall shear stress
Turbulence model coefficients	$C_\mu = 0.069, \kappa = 0.4187$

4.3 Solution method

For the RANS simulations, the discretization equations were solved with the SIMPLEC algorithm, and the discretization schemes for the convection and diffusion terms were a second-order upwind scheme. For the LES and DES simulations, the initial condition was a converged mean flow field generated by a RANS model. The unsteady flow and concentration fields were generated simultaneously. The discretization methods for the pressure and diffusive terms were a second-order upwind scheme, whereas a second-order bounded central-differencing scheme was adopted for the convective term. A second-order implicit scheme was used for temporal discretization. The second order accuracy was maintained through second-order discretization of the momentum, velocity, and temporal terms of the Navier-Stokes equations. Finally, the pressure-velocity coupling method was SIMPLEC. All cases were calculated until the residuals were less than 10^{-5}, and the convergence of each time step in LES and DES simulations was achieved when both the spatially averaged wind speed and CO_2 concentration at the monitor points are stable for several iterations.

Nine LES and DES cases (see Tables 3 and 4) were established with the convergent RNG $k - \varepsilon$ results (see Table 2). Three time step sizes of 0.01, 0.005, and 0.001s were set to investigate the effects of Δt. The non-dimensional form of the time step was defined as $\Delta t^* = \Delta t \times \dfrac{U_H}{H}$ and was used to describe the length of the sampling time, where U_H was the mean inlet speed at the building height and H was the building height. Five values of sampling time $600\Delta t^*$, $1200\Delta t^*$, $1800\Delta t^*$, $2400\Delta t^*$ and $3000\Delta t^*$ (3, 6, 9, 12, and 15s) were selected to evaluate its influence. Furthermore, three ARs of building arrays and two release rates of tracer gas are discussed in Section 6. For unsteady results, the mean field of parameters was calculated from an average over a determined sampling period.

Table 2. Mesh arrangement description of RANS cases.

Case	Grid number	Min size (m)	Turbulence model	CFL	Δt (s)	Δt^*	Sampling length	y^+
RNG-1	3.2 m	0.001	RNG $k - \varepsilon$	—	—	—	—	5.58
RNG-2	5.9 m	0.0005	RNG $k - \varepsilon$	—	—	—	—	2.88
RNG-3	9.4 m	0.00025	RNG $k - \varepsilon$	—	—	—	—	1.45

Table 3. Mesh arrangement description of LES cases.

Case	Grid number	Min size (m)	Turbulence model	CFL	Δt (s)	Δt^*	Sampling length	y^+

LES-1	3.2 m	0.001	LES	1.9	0.005s	0.24	12s	5.32
LES-2	5.9 m	0.0005	LES	1.67	0.005s	0.24	12s	4.22
LES-3	9.4 m	0.00025	LES	1.42	0.005s	0.24	12s	2.27
LES-4	5.9 m	0.0005	LES	3.9	0.01s	0.48	12s	4.67
LES-2	5.9 m	0.0005	LES	1.67	0.005s	0.24	12s	4.22
LES-5	5.9 m	0.0005	LES	0.35	0.001s	0.048	12s	4.42
LES-6	5.9 m	0.0005	LES	1.64	0.005s	0.24	3s	4.22
LES-7	5.9 m	0.0005	LES	1.67	0.005s	0.24	6s	4.22
LES-8	5.9 m	0.0005	LES	1.71	0.005s	0.24	9s	4.31
LES-2	5.9 m	0.0005	LES	1.86	0.005s	0.24	12s	4.55
LES-9	5.9 m	0.0005	LES	1.83	0.005s	0.24	15s	4.51

Table 4. Mesh arrangement description of DES cases.

Case	Grid number	Min size (m)	Turbulence model	CFL	Δt (s)	Δt^*	Sampling length	y^+
DES-1	3.2 m	0.001	DDES	1.35	0.005s	0.24	12s	5.49
DES-2	5.9 m	0.0005	DDES	1.2	0.005s	0.24	12s	3.17
DES-3	9.4 m	0.00025	DDES	0.91	0.005s	0.24	12s	1.65
DES-4	5.9 m	0.0005	DDES	2.12	0.01s	0.48	12s	3
DES-2	5.9 m	0.0005	DDES	1.2	0.005s	0.24	12s	3.17
DES-5	5.9 m	0.0005	DDES	0.24	0.001s	0.048	12s	3.17
DES-6	5.9 m	0.0005	DDES	1.15	0.005s	0.24	3s	3.1
DES-7	5.9 m	0.0005	DDES	1.2	0.005s	0.24	6s	3.17
DES-8	5.9 m	0.0005	DDES	1.21	0.005s	0.24	9s	3.2
DES-2	5.9 m	0.0005	DDES	1.18	0.005s	0.24	12s	3.16
DES-9	5.9 m	0.0005	DDES	1.19	0.005s	0.24	15s	3.12

5. Evaluation of computational parameters

This section evaluates the influences of four computational parameters—turbulence model, grid resolution, discretization of time step size Δt, and length of sampling time—on the predicted flow and concentration fields.

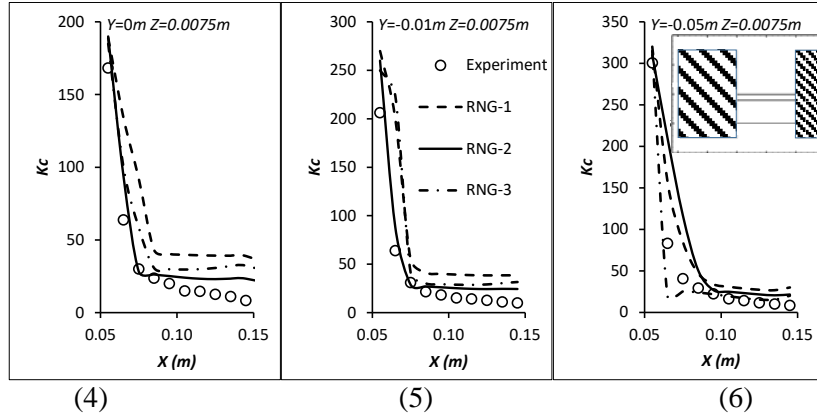5.1 Effects of computational mesh resolution

(1) (2) (3)
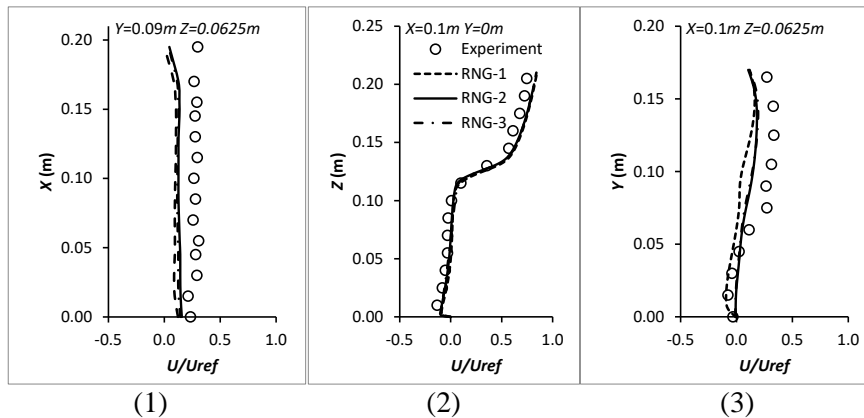
Fig. 4. Mean wind velocity and concentration distribution for coarse, medium, and fine RNG cases as RNG-1, RNG-2, and RNG-3 in Table 2. (1)–(3): mean velocity distribution; (4)–(6): mean concentration distribution.

The mesh resolution tests for the RNG $k - \varepsilon$ model were carried out by cases RNG-1 (coarse mesh), RNG-2 (medium mesh), and RNG-3 (fine mesh) in Table 2. The results, as shown in Fig. 4(1)–(3), show that the wind velocity for the RNG $k - \varepsilon$ model does not vary when the mesh number exceeds a medium grid of 5.9 million ($y^+ = 2.88$) for the building array simulations. Comparing to the wind tunnel results, the velocity component produced by RNG $k - \varepsilon$ appears basically in an acceptable agreement, although there is a slight underestimation of velocity along the longitudinal ($Y = 0.09m, Z = 0.06m$) and horizontal directions ($X = 0.1m, Z = 0.06m$).

Regardless of the acceptable estimation of the velocity component, significant variations are detected in three measured lines, as shown in Fig. 4(6), along the horizontal (X) direction simulated by RNG $k - \varepsilon$ model, as shown in Fig. 4(4)–(6). Also, the finer mesh (RNG-3) does not show better performance of the concentration field than the others (especially RNG-2) when compared to the experimental data. The concentration results of RNG simulations demonstrated overestimations to most parts of the measuring points. This discrepancy might be not only due to the inability of the RNG model to simulate the instantaneous velocity and concentration fields, but also because all of the experimental measurement points were near the ground ($Z = 0.0075m = 0.06H$). Therefore, the case of RNG-2 with the $y^+ = 2.88$ and a minimum grid width of $0.0005m$, is adopted.
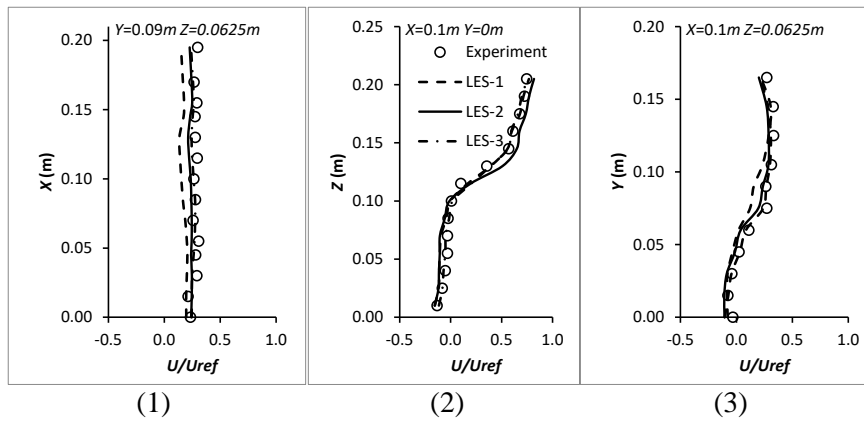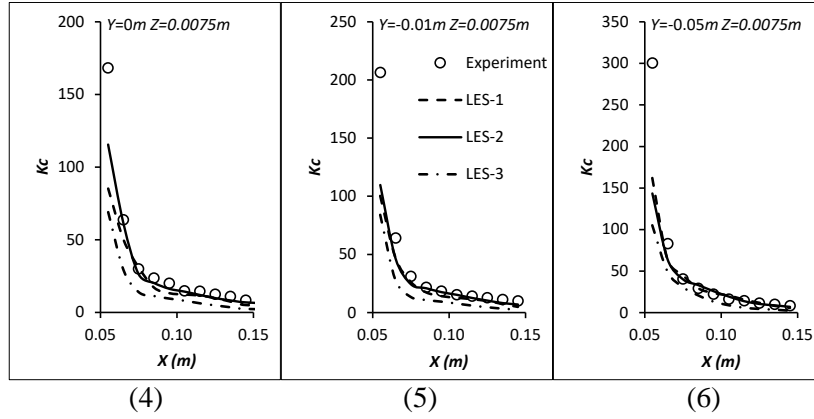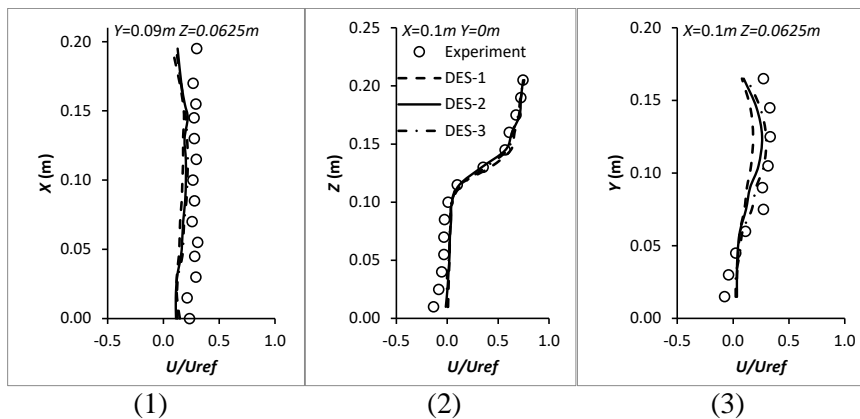
Fig. 5. Mean wind velocity and concentration distributions for coarse, medium, and fine LES cases as LES-1, LES-2, and LES-3 in Table 3. (1)–(3): mean velocity distribution; (4)–(6): mean concentration distribution.

With the same discretization of time step size Δt and sampling period, three densities of meshes (coarse [LES-1], medium [LES-2], and fine [LES-3]) are adopted to test the effects of mesh independence of the LES cases. Fig. 5 presents the non-dimensional wind velocity U^* and the concentration distributions on the leeward side of the target building along three measured lines. For the velocity field, the results of LES-1, which can be seen from Fig. 5(1) and (3), show a slight underestimation relative to the others, and although the results for LES-2 and LES-3 are basically indistinguishable, some minute differences remain. Therefore, a mesh number of 5.9 million ($y^+ = 4.22$) is sufficiently fine to simulate the wind velocity field by LES cases.

However, mass transport is a complex procedure whose accuracy of simulations shows a non-positive correlation with the increase in the mesh number. As shown in Fig. 5(4)–(6), the mesh with 9.4 million grids (LES-3) presents greater underestimations of non-dimensional concentration than LES-1 and LES-2. Some previous studies [50, 63-66] reported similar results that a mesh with more grids does not ensure concentration fields with greater accuracy in LES cases. The modeling and computational errors could mutually compensate to counterbalance each other in some conditions due to their opposite characteristics, which could deplete the whole inaccuracy on a coarser grid system as compared to a finer system. Overall, the grid number of LES-2 ($y^+ = 4.22$) and a minimum grid width of $0.0005m$ is used as compromise choices for numerical accuracy and resources.
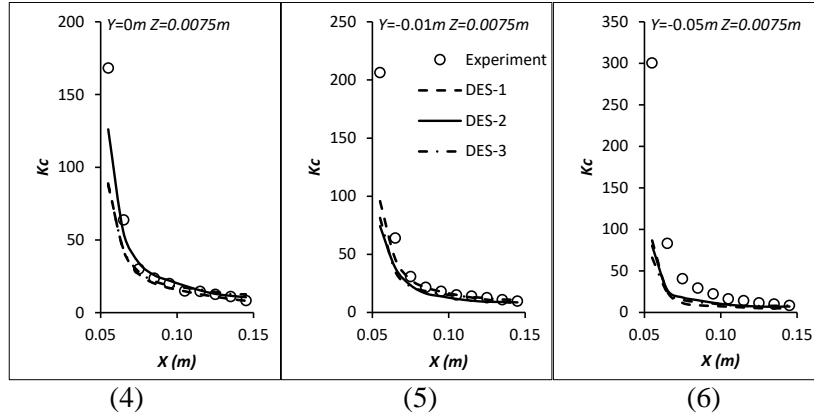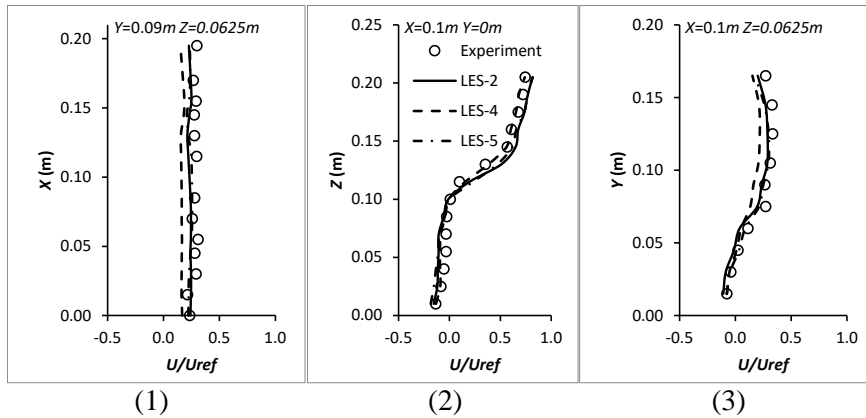

11

Fig. 6. Mean wind velocity and concentration distribution for coarse, medium, and fine DES cases as DES-1, DES-2, and DES-3 in Table 4. (1)–(3): mean velocity distribution; (4)–(6): mean concentration distribution.

Fig. 6 displays the non-dimensional wind velocities and concentrations simulated by the DES model along three measured lines identical to the RNG and LES cases. The velocity and concentration results of DES-2 and DES-3 demonstrate generally the same values, which indicates that the differences become negligible when the mesh number exceeds 5.4 million ($y^+ = 3.17$) for building arrays in DES cases. Although the results of DES-1 do not reveal large differences from the others except for the minor underestimations shown in Fig. 6(3) and (6), the y^+ value of DES-2 ($y^+ = 3.17$) is revealed to be the suitable option in this study. Note that, Kakosimos and Assael [50] observed that the adoption of a more refined mesh in DES model improved the concentration fields significantly; this finding, however, is not manifested by the present study.

5.2 Effect of discretization of time step size Δt and non-dimensional sampling time Δt^*

In unsteady simulations like LES and DES, the appropriate discretization time step size and non-dimensional sampling time are essential to obtain accurate mean fields [61], particularly for parameters with high fluctuations. The non-dimensional sampling time is defined as $\Delta t^* = \Delta t \times \frac{U_H}{H}$, the mean flow and concentration fields are calculated based on averaging within $2400\Delta t^*$, which is 12 s. The Courant-Friedrichs-Lewy (CFL) number [67] is commonly used to indicate the balance between the temporal and spatial scales. The recommended CFL value is around 1 when an explicit solver is used. Three typical discretization time steps are adopted to evaluate the effects of Δt: 0.01, 0.005, and 0.001s.

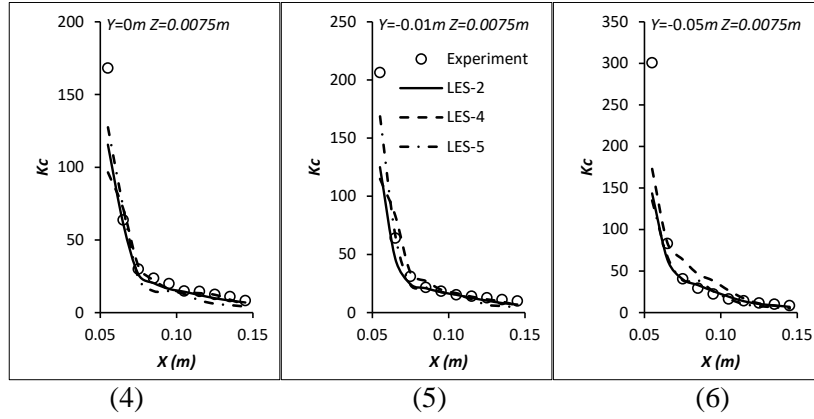(4)   (5)   (6)

Fig. 7. Mean wind velocity and concentration distribution for LES cases with three values of time step size, as LES-2, LES-4, and LES-5 in Table 3. (1)–(3): mean velocity distribution; (4)–(6): mean concentration distribution.

Fig. 7 presents the non-dimensional mean velocity and concentration distribution with three measuring lines for three LES cases (LES-2, LES-4, and LES-5). These three LES cases were calculated with the same mesh number (5.9 million) and sampling time (12s) but with three time step sizes (0.01, 0.005, and 0.0001s). As shown in Fig. 7(1) and (3), the results of LES-4 show subtle underestimations of the wind velocity compared to the experimental data, whereas the results of LES-2 and LES-5 are almost equivalent; in Fig. 7(6), LES-4 shows noticeably larger values than LES-2 and LES-5, whereas the differences between LES-2 and LES-5 are basically inconsequential. This indicates that the effect of the size of the discretization time step on the simulation results becomes insignificant as Δt decreases. Considering that the numerical cost would multiply with a smaller time step size, the size of 0.005s ($\Delta t^* = 0.24$) is chosen as the most provident value for simulation of pollutant dispersion around building arrays.
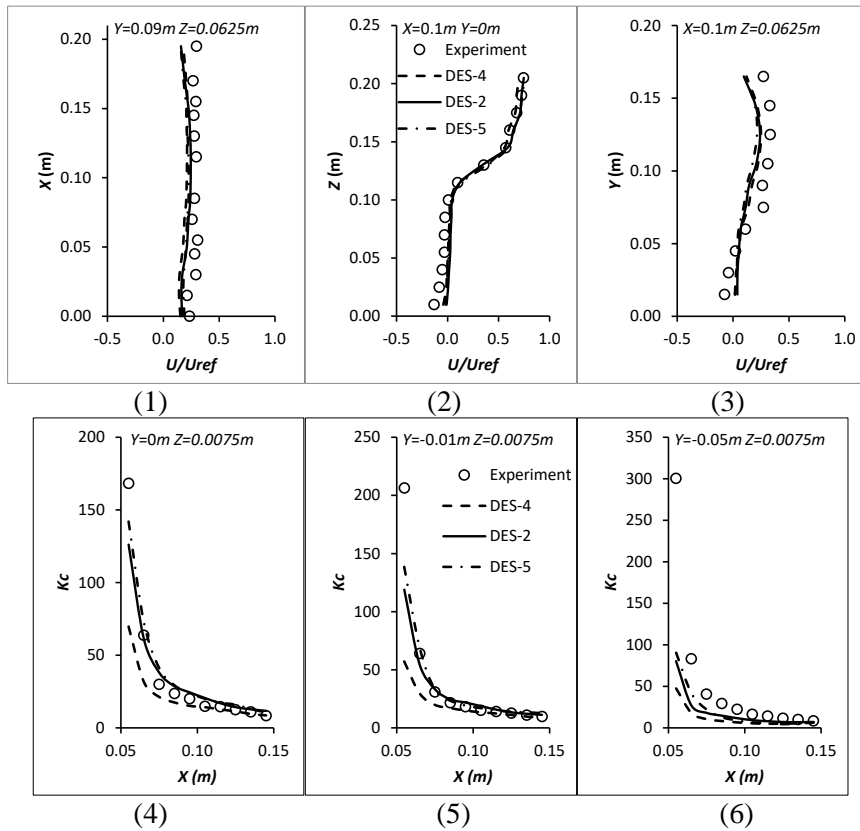

(1)   (2)   (3)

(4)   (5)   (6)

13

Fig. 8. Mean wind velocity and concentration distribution for DES cases with three values of time step size, as DES-2, DES-4, and DES-5 in Table 4. (1)–(3): mean velocity distribution; (4)–(6): mean concentration distribution.

The comparison of different discretization time steps for three DES cases (DES-2, DES-4, and DES-5) are presented in Fig. 8. For the mean velocity fields, the results of the three time steps show limited variance, which means that 0.01s is sufficient to predict the wind distribution around building arrays with the DES model, whereas for the concentration fields, little difference is found between the results of 0.005s and 0.001s; also, compared with the experiment results, the data for 0.01s shows underestimations of most points. Therefore, the time step size of 0.005s ($\Delta t^* = 0.24$) is selected as the compromise value for both velocity and concentration predictions.

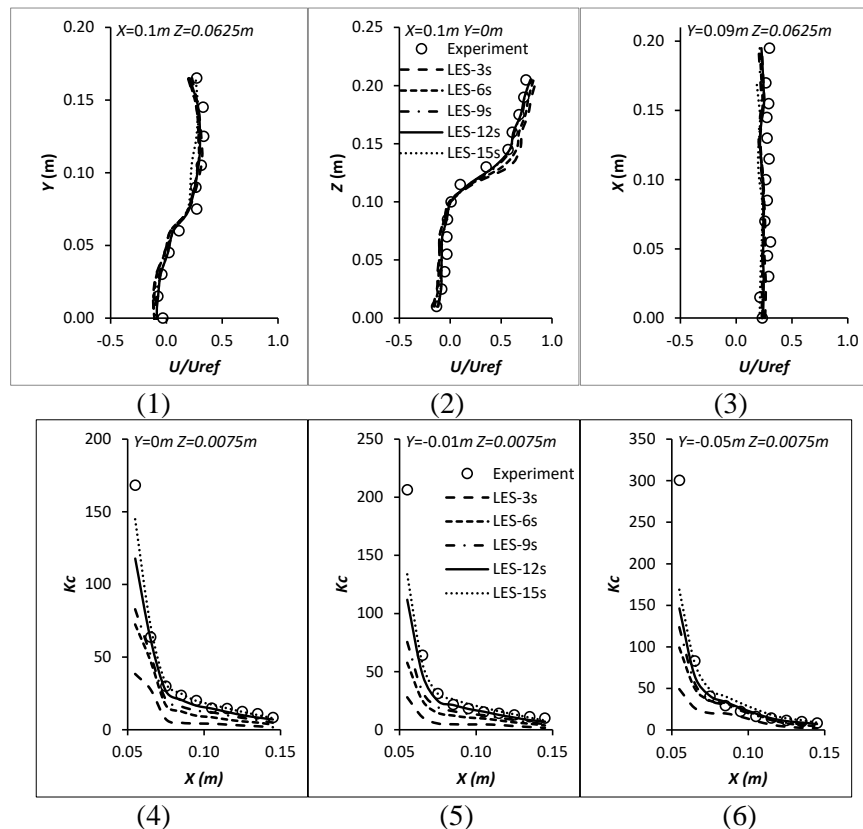(1)   (2)   (3)

(4)   (5)   (6)

Fig. 9. Mean wind velocity and concentration distribution for LES cases with five values of sampling period, as LES-6, LES-7, LES-8, LES-2, and LES-9 in Table 3. (1)–(3): mean velocity distribution; (4)–(6): mean concentration distribution.

Fig. 9 presents the mean velocity and concentration distribution separately along three measuring lines for five LES cases (LES-2, LES-6, LES-7, LES-8, and LES-9). These five LES cases are calculated with the same mesh number (5.9 million) and Δt (0.005s), but with five sampling periods (3, 6, 9, 12, and 15s). The results of the mean velocity field, as presented in Fig. 9(1)–(3), show no differences among the five cases, which indicates that $600\Delta t^*$ (3s) is sufficiently long to produce a steady mean velocity field for building arrays, and the results are unvarying with the increase of the sampling time; however, as shown in Fig. 9(4)–(6), the results for 3, 6, and 9s demonstrate obvious underestimations of the concentration field, whereas the results for 12s and 15s are basically identical to the experimental data, which means that $2400\Delta t^*$ (12s) of sampling time is required to capture a stable concentration distribution around building arrays. This finding can also be detected in an isolated building with LES model [47].
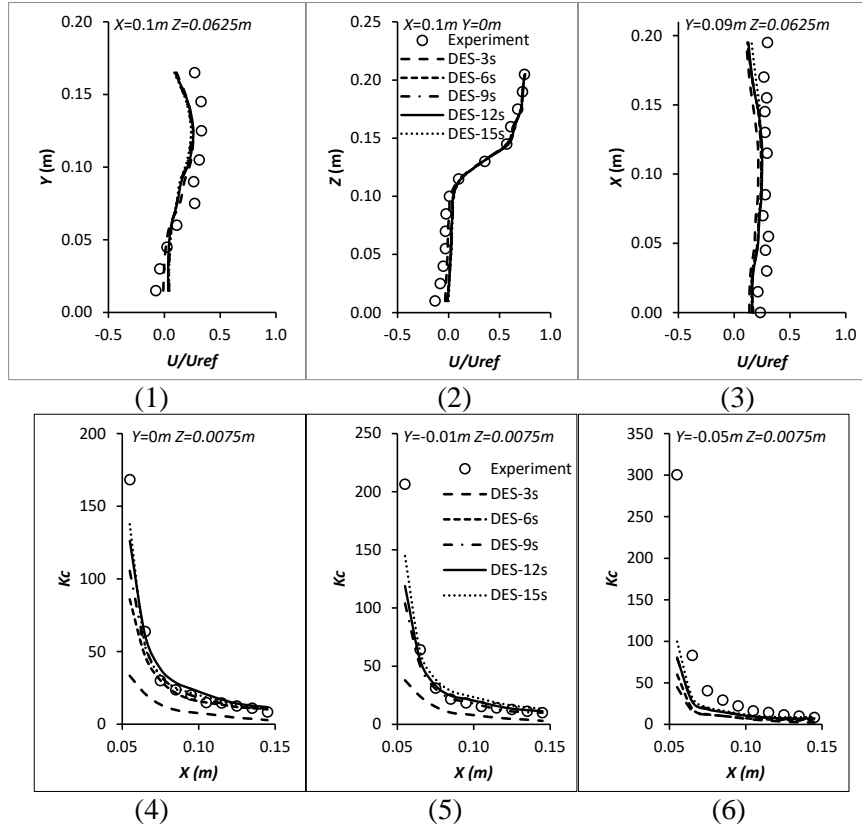
14

Fig. 10. Mean wind velocity and concentration distribution for LES cases with five values of sampling period, as DES-6, DES-7, DES-8, DES-2, and DES-9 in Table 4. (1)–(3): mean velocity distribution; (4)–(6): mean concentration distribution.

The comparison of different sampling times for five DES cases (DES-2, DES-6, DES-7, DES-8, and DES-9) was conducted following a similar procedure as the LES cases, as shown in Fig. 10. The DES results for wind velocity vary little with an increase in sampling time when it exceeds $600\Delta t^*$ (3s); however, for the concentration field, when the sampling time exceeds 6s, the differences are negligible. Therefore, $1200\Delta t^*$ (6s) is sufficiently long to produce the pollutant transportation with the DES model. DES cases predicted stable concentration fields even more quickly than the sampling time of 12s of LES cases because the unsteady RANS model is used in the boundary layer in the DES model, which saves plenty of numerical resources and can obtain stable results faster than the LES model. Convenient for comparisons with LES cases, the results of $2400\Delta t^*$ (12s) are adopted in the next section.

5.3 Comparison of RANS, LES, and DES models

This section presents a comparison of the performance of the three turbulence models in the prediction of velocity and concentration fields in building arrays. In the wind tunnel experiment, the measurement points for the pollutant concentration were at heights of 0.0075 m ($Z = 0.06H$), 1.5 m at the prototype, which was at the pedestrian level.
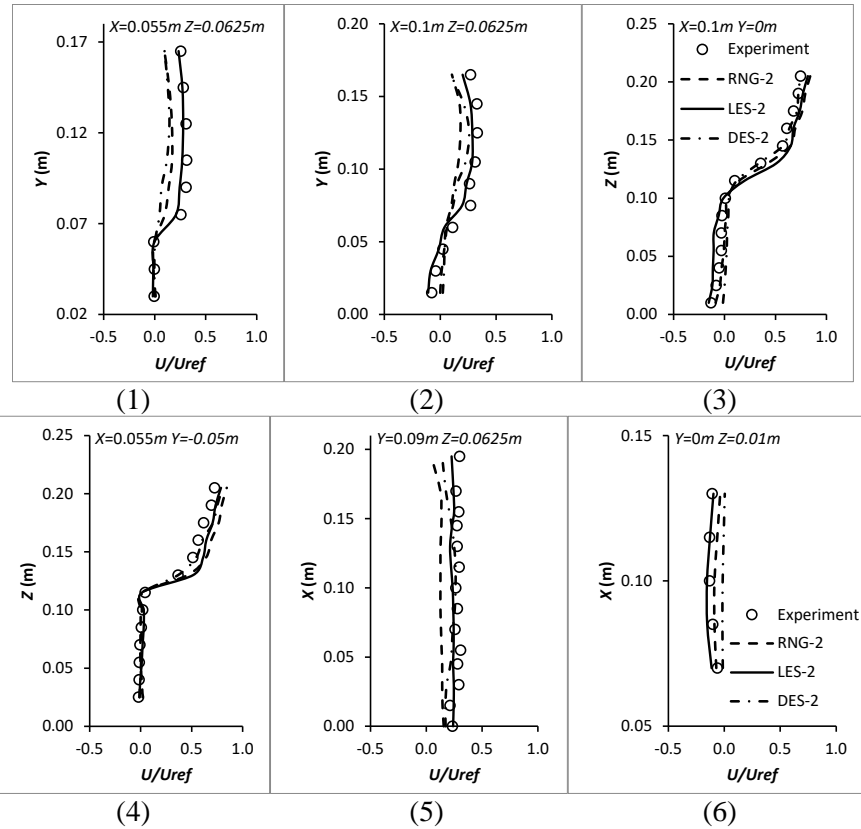
15

Fig. 11 Mean wind velocity distribution for cases of RNG-2, LES-2, and DES-2.

Fig. 11 demonstrates the mean velocity distribution of the RANS, LES, and DES models along six measuring lines on the leeward side of the target building compared to the wind tunnel results. As shown in Fig. 11(3) and (4), along the vertical line (Z direction), three models present similar results and are all in good agreement with the experimental data. However, along the horizontal (X direction) and longitudinal (Y direction) lines, as shown in Fig. 11(1), (2), and (5), RNG-2 and DES-2 both display lower velocities than the wind tunnel data; also, in Fig. 11(6), the reverse flow between the target and the downstream building is underestimated by the two models. In contrast, LES-2 gives more accurate simulations of the mean wind velocity distribution than the RNG and DES models. Although the RNG and DES models simulate only slight underestimations of wind velocity to most parts of the measurement points on the horizontal plane, it may lead to huge discrepancies in the concentration fields.
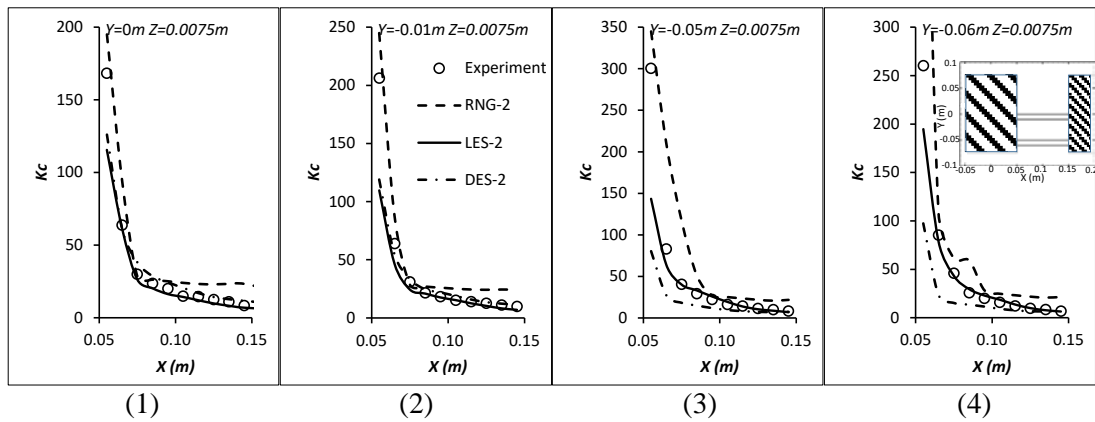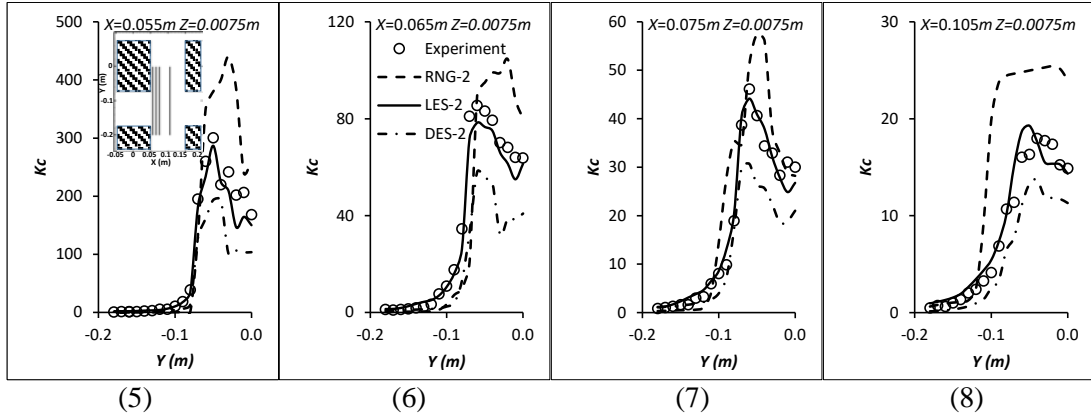
Fig. 12. Mean concentration distribution for cases of RNG-2, LES-2, and DES-2 along lines of horizontal direction (X) and longitudinal direction (Y). (1)–(4): horizontal direction; (5)–(8): longitudinal direction.

Fig. 12(1)–(4) presents the mean concentration along four horizontal lines for the three models, and the relative positions of the four lines are shown in Fig. 12(4). On the leeward side of the target building, the results of the RNG model result in a larger pollutant concentration than the experimental data on almost every measuring point. The LES and DES cases can predict similar results of concentration fields in the middle region, as shown in Fig. 12(1) and (2), which are much closer to the wind tunnel curve than the RNG model. However, in the near-wall area (when X approaches $0.05m$), the LES and DES models both predict lower values for pollutant concentration than the experimental results, and the LES model even shows slightly greater differences than DES, which indicates that both LES and DES models present limited performance of the near-wall region on the leeward side of the target building in predicting the concentration field, even though the wind field simulated by the LES model shows very good agreement with the experimental results. When the measuring lines remain distant from the middle area, as shown in Fig. 12(3) and (4), the performance of the DES model decreases and shows extensive underestimations of the pollutant concentration when compared to the wind tunnel results, but it still yields more stable accuracy than the RNG model.

The mean concentration of four measuring lines of the longitudinal direction (Y) for three models is shown in Fig. 12(5)–(8), and the relative position is shown in Fig. 12(5). The RNG model still predicts much larger concentration values than the experimental data on the leeward of the target building, and it contains a drastic decrease in the concentration for measuring points further from the target building ($Y < -0.1m$), as shown in Fig. 12(6) and (7); this plunge occurs near the lateral boundary of the target building. The performance of the LES model, as shown in Fig. 12(5) and (6), further illustrates that the LES slightly underestimates the pollutant concentration of the near-wall area. However, these underestimations of the concentration values become smaller as the distance from the building wall increases, as shown in Fig. 12(7) and (8). The prediction by the DES model is better than that by the RNG model, as the trends of the simulation curves are basically identical to the LES model and the wind tunnel results. However, substantial underestimations are still given by the DES model for most parts of the measuring area, particularly in the near-wall area on the leeward side of the target building ($Y > -0.1m$). In general, the LES model shows good accordance with the wind tunnel results and is better than both the DES and RNG models in predicting pollutant concentrations; the DES model also predicts more accurate results than the RNG model in some particular areas.
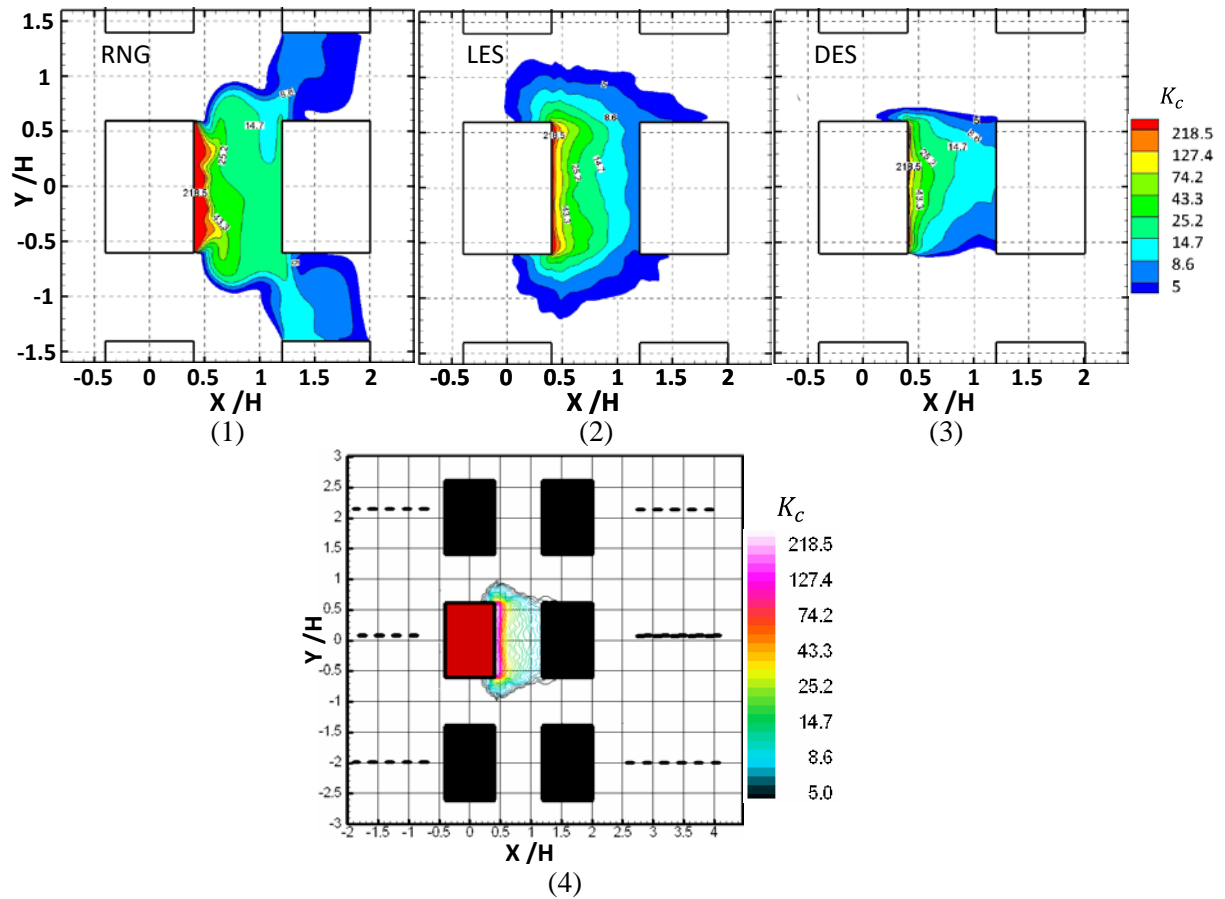
5.4 Mean concentration fields

Fig. 13(1)–(3). Mean concentration contours for cases of RNG-2, LES-2, and DES-2 on the plane of $Z = 0.0075m$; values below 3 are blanked. (4) Mean concentration contour for wind tunnel experiment on the plane of $Z = 0.0075m$ [56].

Fig. 13 shows the contours of the time-averaged dimensionless concentration of the three models and the wind tunnel experiment. On the leeward side of the target building, the high concentration area ($K_c > 218.5$) around the emission vents in RNG model was much larger than experimental results and the LES and DES models. The contours of K_c in the RNG model expand greatly in the leeward region, which could also lead to overvaluation of the pollutant concentration around the downstream buildings. This can be attributed to the underestimation of turbulence diffusion of the RNG model. Compared to the contours predicted by the RNG model, the DES model reveals the opposite situation: that the high concentration region shrank in the near-wall area on the leeward side of the target building. However, the DES model still simulates the concentration field better than the RNG model when compared with the wind tunnel results, and it provides acceptable prediction of mean concentrations on the latter half between the target and downstream building, which is also demonstrated in Fig. 12(3) and (4). Unlike the DES and RNG models, the general pollutant distribution of K_c generated by LES is very similar to that of the experiment, although the margin of the LES contour trends to be diffusive.

In the RNG model, as shown in Fig. 13(1), the pollutants emitted from the target building are mainly transferred downstream, which leads to smaller values for the pollutant concentration than those of the LES model on both lateral sides of the target building. The DES model also reveals similar underestimations of the pollutant distribution on the lateral sides, as shown in Fig. 13(3). This finding can be explained by the coarser mesh grids on the lateral sides of the target building than those on the leeward side, which triggers the DES model to switch to the unsteady RANS model in this area and to obtain results similar to those of the RNG model.
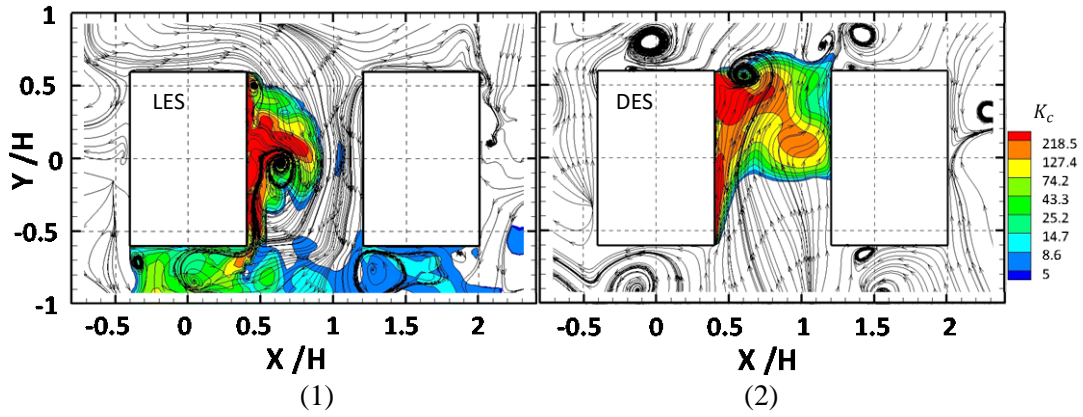
Fig. 14 Instantaneous concentration contours and wind streamlines for cases of LES-2 and DES-2 at the instant time of $2400\Delta t^*$ on the plane of $Z = 0.0075m$, values below 3 are blanked.

Fig. 14 shows the instantaneous concentration dispersion and wind flow structures predicted by LES and DDES models at an instant momentum of $2400\Delta t^*$. The detailed concentration contours and wind patterns are convoluted and irregular, which barely show the gradual reduction away from the emission as Fig. 13. The highly fluctuated vortices guide the pollutant transported pathway to concentrate in the wake region of the target building. In addition, the concentration contour predicted by DDES model shows smaller area of pollutant distribution and high concentration ($K_c > 25.2$) than LES model. It also reveals that the DDES model underestimates the pollutant diffusion around the building arrays.

Overall, the LES model predicts the close distribution of the pollutant concentration around building arrays to the wind tunnel results, whereas the accuracy of the DES simulation is accepted in part of the diffusion region.
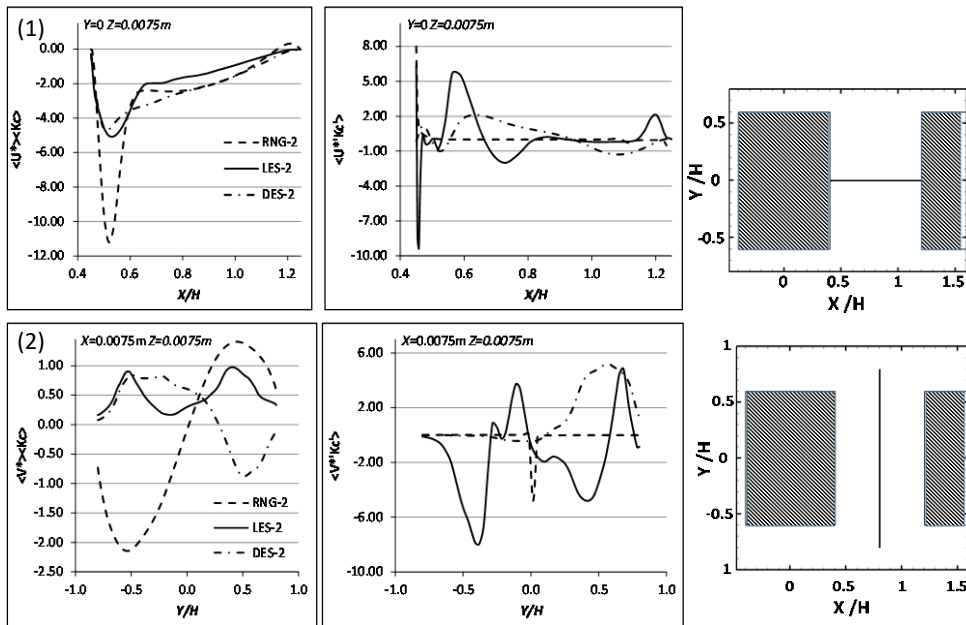
5.5 Concentration fluxes

Fig. 15(1). Comparison of X and components of convective fluxes $\langle U^* \rangle \langle K_c \rangle$ and turbulent mass fluxes $\langle U^{*'} K_c' \rangle$ of three turbulence models. (2) Comparison of Y components of convective fluxes $\langle V^* \rangle \langle K_c \rangle$ and turbulent mass fluxes $\langle V^{*'} K_c' \rangle$ of three turbulence models.

The mass transport is essentially represented by the distribution of concentration fluxes, which can provide significant information on the certainty of an adopted model for concentration transport. The scalar transport of the concentration contains convective and turbulent fluxes, which are defined as

19

mean convective fluxes $\langle U^* \rangle \langle K_c \rangle$ and turbulent mass fluxes $\langle U^{*\prime} K_c{}^\prime \rangle$, respectively [43, 46, 50, 68]. The convective fluxes at a specific point can be calculated by the product of the local mean velocity and the mean concentration; it is $\langle U^* \rangle \langle K_c \rangle$ for the horizontal (X) direction and $\langle V^* \rangle \langle K_c \rangle$ for the longitudinal (Y) direction. The terms U^* and V^* are nondimensional velocity components. The turbulent diffusion fluxes are given by $\langle U^{*\prime} K_c{}^\prime \rangle$ in the LES and DES models, but they are calculated with the gradient-diffusion hypothesis in the RANS model, which is $\langle U^{*\prime} K_c{}^\prime \rangle = -\frac{\nu_t}{Sc_t}\frac{\partial K_c}{\partial x_i}$, where ν_t is the eddy viscosity, and Sc_t is the turbulent Schmidt number.

Fig. 15(1) compares the horizontal (X) components of the convective flux and turbulent diffusion flux in the middle line of the leeward side of the target building. The negative value of $\langle U^* \rangle \langle K_c \rangle$ of the RNG model is much larger than those of the LES and DES models, which means that the RNG model predicted a stronger reverse flow near the ground on the leeward side of the target building than the others. The magnitude of the reverse flow of the DES model is similar to that of the LES model, but the turbulent fluxes $\langle U^{*\prime} K_c{}^\prime \rangle$ in the LES model show larger values than those in the RNG and DES models, and the negative peak value occurs near the emission vent. The positive peak value of the RNG model is smaller than that of the LES model.

Fig. 15(2) shows the longitudinal (Y) components of convective flux $\langle V^* \rangle \langle K_c \rangle$ and turbulent flux $\langle V^{*\prime} K_c{}^\prime \rangle$ along the measuring line in the middle between the target and the downstream building. The peak values of the convective fluxes of the three models show different signs because the flow directions of the measuring line are opposite in the three models. The LES model predicts the same wind direction along the measuring line, whereas the RNG and DES models show two mutually opposite directions. Furthermore, considerable differences among three models are observed in the distribution of turbulent flux. The RNG model result shows a negative peak around the middle of the measuring line ($Y = 0$), which is the transitional point of the convective flux. However, in the LES and DES models, the curves of turbulent fluxes are in opposite signs with convective fluxes, which means that the longitudinal component fluxes can be balanced out in the LES and DES models. The good agreement with the wind tunnel results of the mean concentration distribution, as shown in Fig. 12, indicates that the concentration fluxes simulated by the LES model can reproduce the mass transport more accurately than the DES and RNG models.
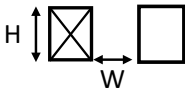
6. Evaluation of physical parameters

This section evaluates the influences of physical parameters, including the AR of the building arrays and the release rate of the tracer gas on the concentration fields. It adopts the combination of numerical settings from Section 5, which are 0.005s ($\Delta t^* = 0.24$) of time step size Δt and 12s ($2400\Delta t^*$) of sampling length in the LES model. Other numerical settings, such as the boundary conditions and solution methods, are identical to the settings in Section 4.

6.1 Effect of aspect ratio

Regarding aspect ratios of 0.5, 1.0, 1.25, and 2.0, this section evaluates the effect of ARs on the prediction of pollutant transport among the building arrays. The configurations of ARs of 0.5, 1.0, 1.25, and 2.0 are described in Table 5.

Table 5. Aspect ratio descriptions of building arrays.

	H/W	AR	Plots
Experiment	0.125/0.1	1.25	

AR=0.5	0.125/0.25	0.5	H ↕ ⊠ ← → □ W
AR=1	0.125/0.125	1.0	H ↕ ⊠ ←→ □ W
AR=2	0.125/0.0625	2.0	H ↕ ⊠ ← □ W

Because the various aspect ratios of building arrays change the flow regime essentially, the pollutant transportation will also be modified drastically. Fig. 15 demonstrates the non-dimensional concentration of eight measuring lines for the four AR cases. The relative position (X/W) is adopted to illustrate the pollutant distribution on the leeward side of the target building. The positions of the eight lines are shown in Fig. 16(4). As shown in Fig. 16, the cases with ARs of 0.5, 1, and 1.25 display similar curves, which shows that the wind flow pattern does not change as the AR increases. The results with ARs of 0.5, 1, and 1.25 also showed relatively stable growth of the concentration values, which could indicate that the pollutants on the leeward side of the target building will accumulate as the AR increases from 0.5 to 1.25. The results with an AR of 0.5 remain the smallest values because the situation with a wider street shows more efficient dilution. However, the results with an AR of 2 do not show consistently larger values than ARs of 1 and 1.25. On the contrary, when the measuring points are in the middle of the leeward side of the target building and close to the emitting sources, the non-dimensional concentration of an AR of 2 presents restricted lower values than ARs of 1 and 1.25, as shown in Fig. 16(1), (2), (6), and (7); however, as the measuring points move away from the middle, the results with an AR of 2 remain largest, as seen in Fig. 16(4). Also, as shown in Fig. 16(5)–(8), the peak values of concentration of the four cases occur near the position $Y = -0.06m$, where the case with an AR of 2 holds a much larger peak concentration than others. These phenomena illustrate that the wind flow field in this case does not follow a pattern similar to that with an AR below 1.25 and leads to greater dilution of the pollutants near the emitting source. There is likely a certain AR below which the accumulation is dominant as the AR increases and above which dilution and accumulation conflict with each other and result in a lower concentration of specific areas.
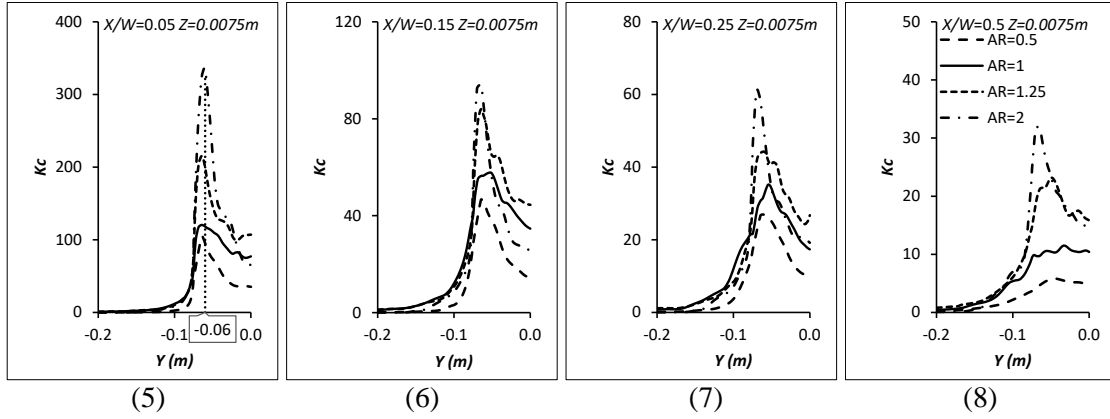

(1)   (2)   (3)   (4)
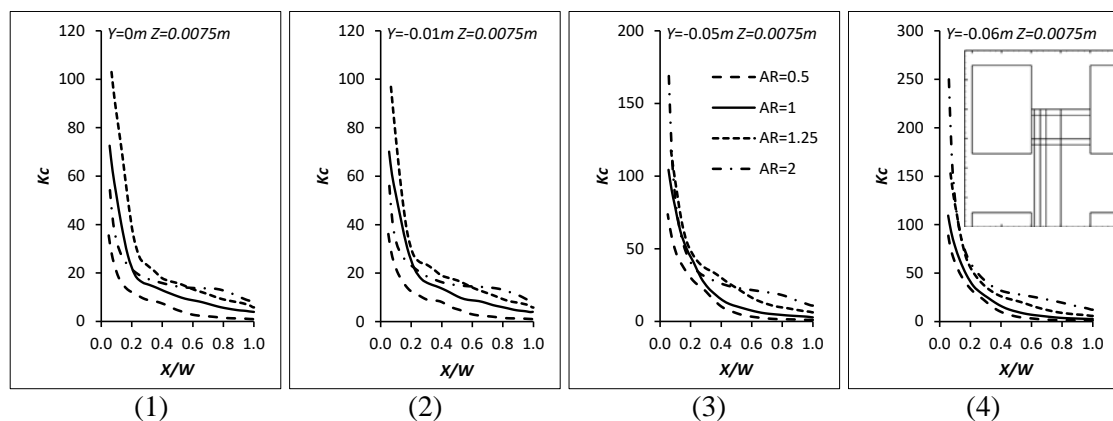
Fig. 16. Non-dimensional concentration K_c for ARs of 0.5, 1, and 2 along eight measuring lines; (1)–(4) are in the Y direction and (5)–(8) are in the X direction.
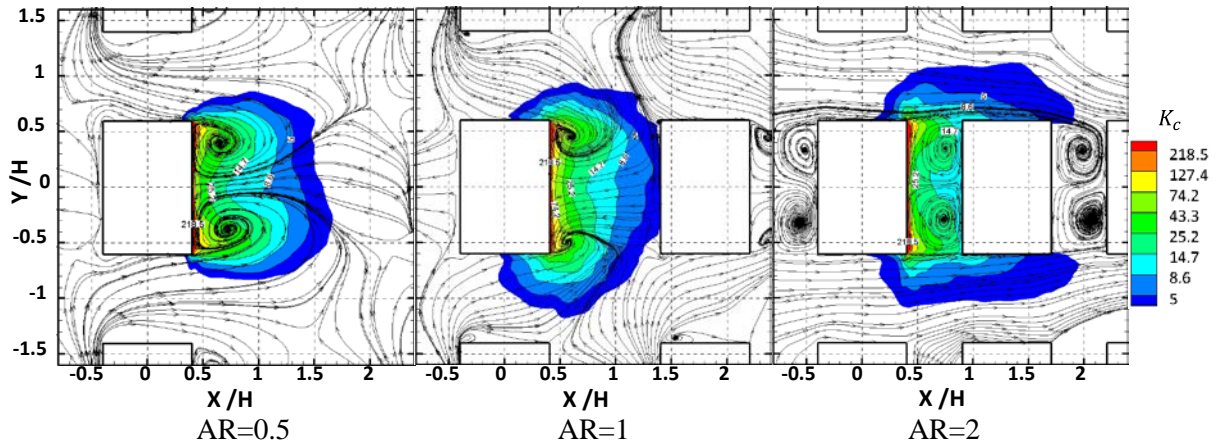

Fig. 17. Mean concentration contours and velocity streamlines for ARs of 0.5, 1, and 2 on the plane of $Z = 0.0075m$; values below 2 are blanked.

Fig. 17 shows the mean concentration contours and streamlines of ARs of 0.5, 1, and 2 on the plane of $Z = 0.0075m$. When the width between the target and the downstream building decreases, the wind flow field changes, especially on the lateral sides. The wind flows directly downstream on the lateral sides with an AR of 2, instead of forming vortices on the leeward side of the target building as in the cases with ARs of 0.5 and 1, which causes relatively low concentration values on the lateral sides for an AR of 2 than for an AR of 1. The low interaction of wind fluctuations between the lateral and leeward sides also causes a much higher peak value near the margin of the building in the case with an AR of 2. Furthermore, because it is blocked by the downstream building, the pollutant can be transported a longer distance with an AR of 2. In contrast, with an AR of 0.5, the greater width introduces high fluctuations that make the pollutant dilute more quickly than others and leads to lower non-dimensional concentration values.

Generally, different characteristics in transporting pollutants can be detected in these four cases. When the AR is below 1.25, a linear increase is observed in the concentration; but for a narrower street canyon (e.g., with an AR of 2), the pollutant dispersion pattern is changed and no longer follows a linear increase with AR. This finding implies that a transition value of AR in building arrays exists between 1.25 and 2. If the width of the street decreases further (e.g., an AR of 3), transporting patterns similar to those with an AR of 2 may be found. However, there may be another AR above which dilution will predominate and cause different dispersion patterns that should be investigated in a future study. Because the wind flow field with a large AR shows distinct peculiarities, other experiments should also be conducted to target larger ARs in building arrays.

6.2 Effect of pollutant release rate

The releasing rate of pollutants may influence the dispersion characteristics in building arrays. However, few previous studies examined such an influence in a quantitative manner. Based on the experimental model, this section evaluates the effects of the release rates of tracer gas on the pollutant distributions in the building arrays. Table 6 presents the examined release rates.

Table 6. Pollutant release rate descriptions of building arrays.

	Release rate	Ratio
Experiment	$1.15 \times 10^{-5}\ m^3/s$	1
RR-2	$2.23 \times 10^{-5}\ m^3/s$	2
RR-5	$5.75 \times 10^{-5}\ m^3/s$	5

Fig. 18 compares the pollutant concentration results with the various release rates of the tracer gas CO_2. The mean concentration of CO_2 along the measuring lines increases as the release rate increases, as shown in Fig. 18(1)–(4). Because one of the pollutant sources is located on the position $Y = -0.065m$, the pollutant concentration around the opening responds dramatically to the increase in the release rate, as shown in Fig. 18(1) and (4). Similar phenomena can be found near the pollutant source on the leeward wall of the target building ($X = -0.05m$). However, regarding the non-dimensional concentration K_c, the discrepancies among the release rates are not very obvious, particularly in the middle on the leeward side of the target building, as shown in Fig. 18(6) and (7). However, in Fig. 18(5) and (8), the results of RR-2 present larger values than RR-5, which can be attributed to the fact that the mean concentration in the sources of RR-5 is much larger than that of RR-2 and leads to the smaller value of K_c. It also implies that the concentration level does not increase linearly as the source concentration increases, possibly because the higher release rate comes with the higher release speed. With the higher release speed, the release momentum pushes the tracer gas further, which results in a lower concentration in the areas near the source.
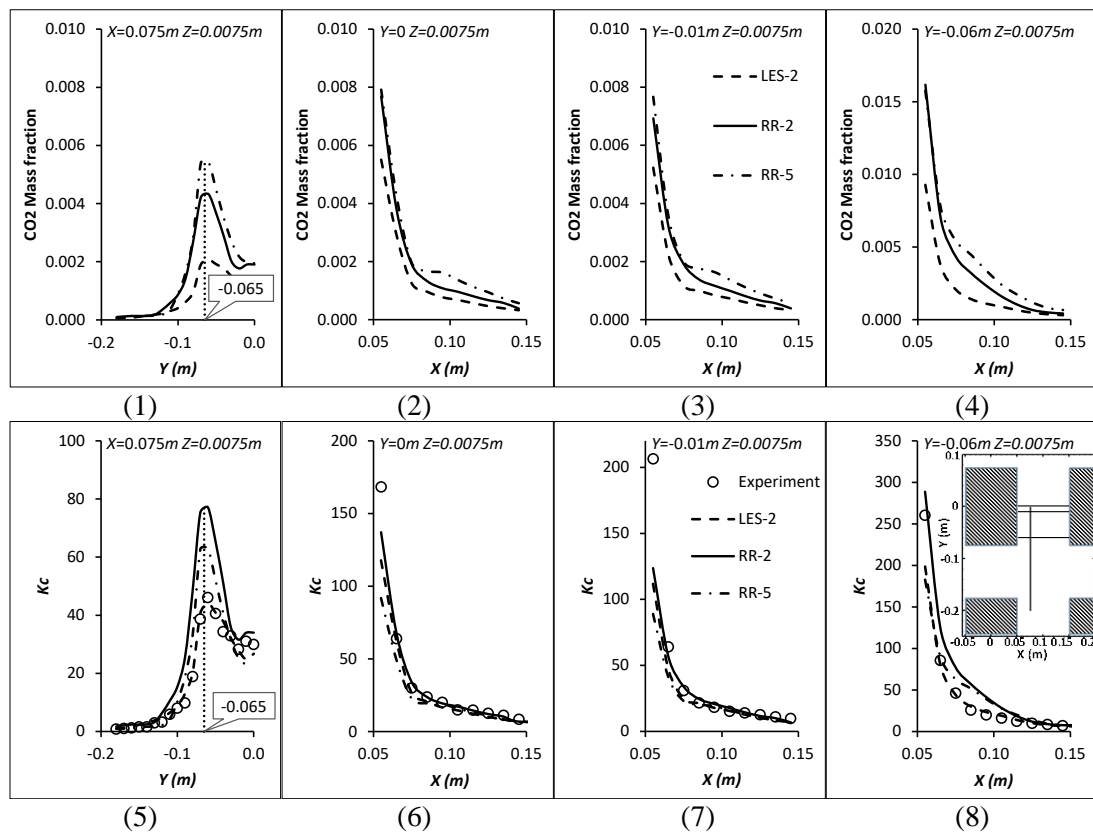
Fig. 18. CO_2 mass fraction and non-dimensional concentration K_c for cases of LES-2, RR-2, and RR-5 along four measuring lines; (1)–(4) are CO_2 mass fraction and (5)–(8) are non-dimensional concentration K_c.

Fig. 19 demonstrates the time-averaged dimensionless concentration contours of various release rates. As the release rate increases, the area of high concentration ($K_c > 25.2$) remains; but the low concentration area ($K_c < 25.2$) grows larger, especially with RR-5, which infers that a higher concentration in the source will contaminate a larger region in the building array, although it does not alter the basic transportation of gaseous pollutants. It further illustrates that the higher release rate of tracer gas causes an increase in the release momentum and also leads to a lower concentration near the emitting source.

Overall, the increase in the release rate of the tracer gas does not change the basic characteristics of pollutant dispersion in the building array, but the concentration level does not increase linearly with the increase in the source concentration. With the higher release rate, the release momentum drives the tracer gas to disperse more efficiently, which results in a lower concentration in the areas near the source and a longer distance.
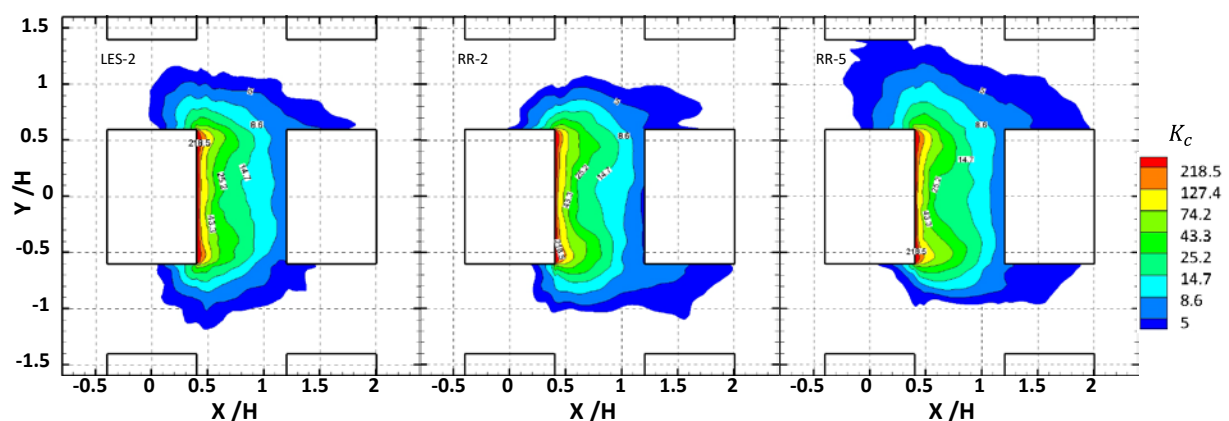

Fig. 19. Mean concentration contours for cases of LES-2, RR-2, and RR-5 on the plane of $Z = 0.0075m$; values below 3 are blanked.

7. Conclusions

This study centers on the problem of accurate prediction of pollutant dispersion in building arrays using a CFD method, focusing on evaluation of the influence of four computational and two physical parameters. These parameters include three turbulence models (RNG, LES, and DES), mesh resolution, discretization of time step sizes, sampling lengths, aspect ratios and release rates of tracer gas. A set of wind tunnel experimental data was used as a baseline for the evaluations. The results can be summarized as follows.

(1) With the LES and DES models, when Δt^* is lower than 0.24 ($\Delta t = 0.005\ s$), the discretization of the time step size has minute and inconsequential effects on the results of both velocity and pollutant fields in the building arrays.

(2) For wind velocity fields, a sampling length of $600\ \Delta t^*$ (3s) is adequate; but for concentration fields, the sampling time is much longer, $2400\ \Delta t^*$ (12s) for LES cases and $1200\ \Delta t^*$ (6s) for DES cases, respectively. The DES model needs less sampling time than the LES model to obtain stable concentration fields under same mesh number and discretization of time step size.

(3) The mean velocity fields predicted by the RNG, LES, and DES models are all in good agreement with the wind tunnel results along the vertical (Z) direction, but the LES model shows better performance along the horizontal (X) and longitudinal (Y) directions. For the concentration fields, the three models perform quite differently. The RNG model predicts much higher results on the leeward side of the target building and underestimates the distributions on

24

the lateral sides. The DES model produces acceptable results in some specific areas but underestimates most parts of the testing area. The LES model predicts the most accurate pollutant distribution fields compared to the wind tunnel results, but in areas near the source, its performance is ordinary, but still better than the RNG and DES models.

(4) Different characteristics in transporting pollutants can be detected under four aspect ratios (0.5, 1, 1.25, and 2). With an AR of 2, the pollutant dispersion pattern does not follow a linear increase as with ARs below 1.25, which implies that a transition value of AR in building arrays exists between 1.25 and 2. An increase in the AR will causes the dilution and accumulation effects to interact. Because a larger AR shows different peculiarities, more experiments with pollutant dispersion in building arrays need be conducted with larger ARs.

(5) An increase in the release rate of tracer gas does not drastically change the basic characteristics of gas transportation in building arrays. However, the concentration level does not increase linearly with the source concentration. Due to the greater release momentum caused by the higher release rate, the tracer gas can pollute larger fields and show an unexpectedly lower concentration near the emitting sources.

Acknowledgement

References

1 Handbook, A., *ASHRAE Handbook–Fundamentals.* Atlanta, GA, 2009.
2 Pasquil, F.S., and Smith, F.B., *Atmospheric diffusion.* 1983.
3 Handbook, A., *HVAC applications.* ASHRAE Handbook, Fundamentals, 2007(2003).
4 Ashrae, H., *HVAC Applications Handbook.* SI Edition, 2011.
5 Drivas, P.J. and Shair, F.H., *Probing the air flow within the wake downwind of a building by means of a tracer technique.* Atmospheric Environment (1967), 1974. **8**(11): p. 1165-1175.
6 Wilson, D.J. and Lamb, B.K., *Dispersion of exhaust gases from roof-level stacks and vents on a laboratory building.* Atmospheric Environment, 1994. **28**(19): p. 3099-3111.
7 Stathopoulos, T., Lazure, L., Saathoff, P. and Gupta, A., *The effect of stack height, stack location and rooftop structures on air intake contamination.* A laboratory and full-scale study, 2004.
8 Stathopoulos, T., Hajra, B. and Bahloul, A., *Analytical evaluation of dispersion of exhaust from rooftop stacks on buildings*. 2000: Institut de recherche Robert-Sauvé en santé et en sécurité du travail.
9 Yassin, M.F., Kato, S., Ooka, R., Takahashi, T. and Kouno, R., *Field and wind-tunnel study of pollutant dispersion in a built-up area under various meteorological conditions.* Journal of Wind Engineering and Industrial Aerodynamics, 2005. **93**(5): p. 361-382.
10 Santos, J.M., Reis, N.C., Goulart, E.V. and Mavroidis, I., *Numerical simulation of flow and dispersion around an isolated cubical building: The effect of the atmospheric stratification.* Atmospheric Environment, 2009. **43**(34): p. 5484-5492.
11 Finn, D., Clawson, K.L., Carter, R.G., Rich, J.D., Biltoft, C. and Leach, M., *Analysis of Urban Atmosphere Plume Concentration Fluctuations.* Boundary-Layer Meteorology, 2010. **136**(3): p. 431-456.
12 Baldauf, R.W., Heist, D., Isakov, V., Perry, S., Hagler, G.S., Kimbrough, S., Shores, R., Black, K. and Brixey, L., *Air quality variability near a highway in a complex urban environment.* Atmospheric Environment, 2013. **64**(Supplement C): p. 169-178.
13 Li, W. W. and Meroney, R.N., *Gas dispersion near a cubical model building. Part II. Concentration fluctuation measurements.* Journal of Wind Engineering and Industrial Aerodynamics, 1983. **12**(1): p. 35-47.

14 Poreh, M. and Cermak, J.E., *Small scale modeling of line integrated concentration fluctuations.* Journal of Wind Engineering and Industrial Aerodynamics, 1990. **36**(Part 1): p. 665-673.

15 Higson, H.L., Griffiths, R.F. and Jones, C.D., *Concentration measurements around an isolated building: A comparison between wind tunnel and field data.* Atmospheric Environment, 1994. **28**(11): p. 1827-1836.

16 Meroney, R.N., Leitl, B., Rafailidis, S. and Schatzmann, M., *Wind-tunnel and numerical modeling of flow and dispersion about several building shapes.* Journal of Wind Engineering and Industrial Aerodynamics, 1999. **81**(1): p. 333-345.

17 Schatzmann, M., Leitl, B., and Liedtke, J., *Dispersion in Urban Environments*, in *Urban Air Quality: Measurement, Modelling and Management: Proceedings of the Second International Conference on Urban Air Quality: Measurement, Modelling and Management Held at the Computer Science School of the Technical University of Madrid 3–5 March 1999*, R.S. Sokhi, et al., Editors. 2000, Springer Netherlands: Dordrecht. p. 249-257.

18 Moonen, P., Defraeye, T., Dorer, V., Blocken, B. and Carmeliet, J., *Urban Physics: Effect of the micro-climate on comfort, health and energy demand.* Frontiers of Architectural Research, 2012. **1**(3): p. 197-228.

19 Sini, J.-F., Anquetin, S. and Mestayer, P.G., *Pollutant dispersion and thermal effects in urban street canyons.* Atmospheric Environment, 1996. **30**(15): p. 2659-2677.

20 Barlow, J.F. and Coceal, O., *A review of urban roughness sublayer turbulence.* Met Office Research and Development–Technical Report, 2009. **1**: p. 527.

21 Leitl, B., Kastner-Klein, P., Rau, M. and Meroney, R.N., *Concentration and flow distributions in the vicinity of U-shaped buildings: wind-tunnel and computational data.* Journal of Wind Engineering and Industrial Aerodynamics, 1997. **67**: p. 745-755.

22 Ai, Z.T. and Mak C.M., *Analysis of fluctuating characteristics of wind-induced airflow through a single opening using LES modeling and the tracer gas technique.* Building and environment, 2014. **80**: p. 249-258.

23 Ai, Z.T. and Mak C.M., *Determination of single-sided ventilation rates in multistory buildings: Evaluation of methods.* Energy and Buildings, 2014. **69**: p. 292-300.

24 Cui, D.J., Mak, C.M., Kwok, K.C. and Ai, Z.T., *CFD simulation of the effect of an upstream building on the inter-unit dispersion in a multi-story building in two wind directions.* Journal of Wind Engineering and Industrial Aerodynamics, 2016. **150**: p. 31-41.

25 Huang, Y., Hu, X. and Zeng, N., *Impact of wedge-shaped roofs on airflow and pollutant dispersion inside urban street canyons.* Building and Environment, 2009. **44**(12): p. 2335-2347.

26 Gousseau, P., Blocken, B., Stathopoulos, T. and Van Heijst, G., *CFD simulation of near-field pollutant dispersion on a high-resolution grid: a case study by LES and RANS for a building group in downtown Montreal.* Atmospheric Environment, 2011. **45**(2): p. 428-438.

27 Tominaga, Y. and Stathopoulos, T., *CFD simulation of near-field pollutant dispersion in the urban environment: A review of current modeling techniques.* Atmospheric Environment, 2013. **79**(Supplement C): p. 716-730.

28 Tominaga, Y. and Stathopoulos, T., *Ten questions concerning modeling of near-field pollutant dispersion in the built environment.* Building and Environment, 2016. **105**: p. 390-402.

29 Lateb, B.M., et al., *On the use of numerical modelling for near-field pollutant dispersion in urban environments − A review.* Environmental Pollution, 2016. **208**(Part A): p. 271-283.

30 Chan, T.L., et al., *Validation of a two-dimensional pollutant dispersion model in an isolated street canyon.* Atmospheric Environment, 2002. **36**(5): p. 861-872.

31 Blocken, B., Meroney, R.N., Yataghenem, M., Fellouah, H., Saleh, F. and Boufadel, M.C., *Numerical evaluation of pollutant dispersion in the built environment: comparisons between models and experiments.* Journal of Wind Engineering and Industrial Aerodynamics, 2008. **96**(10): p. 1817-1831.

32 Tominaga, Y. and Stathopoulos, T., *Numerical simulation of dispersion around an isolated cubic building: Comparison of various types of k–ε models.* Atmospheric Environment, 2009. **43**(20): p. 3200-3210.

33 Nazridoust, K. and Ahmadi, G., *Airflow and pollutant transport in street canyons.* Journal of wind engineering and industrial aerodynamics, 2006. **94**(6): p. 491-522.

34 Yakhot, V., Orszag, S., Thangam, S., Gatski, T. and Speziale, C., *Development of turbulence models for shear flows by a double expansion technique.* Physics of Fluids A: Fluid Dynamics (1989-1993), 1992. **4**(7): p. 1510-1520.

35 Dai, Y.W., Mak, C.M. and Ai, Z.T., *Computational fluid dynamics simulation of wind-driven inter-unit dispersion around multi-storey buildings: Upstream building effect.* Indoor and Built Environment. **0**(0): p. 1420326X17745943.

36 Shih, T.H., Liou, W.W., Shabbir, A., Yang, Z. and Zhu, J., *A new k-ϵ eddy viscosity model for high reynolds number turbulent flows.* Computers & Fluids, 1995. **24**(3): p. 227-238.

37 Launder, B.E. and Spalding, D.B., *Mathematical models of turbulence.* 1972: Academic press.

38 Chang, C.H. and Meroney, R.N., *Numerical and physical modeling of bluff body flow and dispersion in urban street canyons.* Journal of Wind Engineering and Industrial Aerodynamics, 2001. **89**(14): p. 1325-1334.

39 Hang, J., Li, Y., Sandberg, M., Buccolieri, R. and Di Sabatino, S., *The influence of building height variability on pollutant dispersion and pedestrian ventilation in idealized high-rise urban areas.* Building and Environment, 2012. 56, pp.346-360.

40 Yuan, C., Ng, E. and Norford, L.K., I*mproving air quality in high-density cities by understanding the relationship between air pollutant dispersion and urban morphologies.* Building and Environment, 2014. 71, pp.245-258.

41 Murakami, S., *Comparison of various turbulence models applied to a bluff body.* Journal of Wind Engineering and Industrial Aerodynamics, 1993. **46**(Supplement C): p. 21-36.

42 Mochida, A. and Lun, I.Y.F., *Prediction of wind environment and thermal comfort at pedestrian level in urban area.* Journal of Wind Engineering and Industrial Aerodynamics, 2008. **96**(10): p. 1498-1527.

43 Tominaga, Y. and Stathopoulos, T.,*Numerical simulation of dispersion around an isolated cubic building: model evaluation of RANS and LES.* Building and Environment, 2010. **45**(10): p. 2231-2239.

44 Tominaga, Y. and Stathopoulos, T., *CFD modeling of pollution dispersion in a street canyon: Comparison between LES and RANS.* Journal of Wind Engineering and Industrial Aerodynamics, 2011. **99**(4): p. 340-348.

45 Tominaga, Y. and Stathopoulos, T., *CFD modeling of pollution dispersion in building array: evaluation of turbulent scalar flux modeling in RANS model using LES results.* Journal of Wind Engineering and Industrial Aerodynamics, 2012. **104**: p. 484-491.

46 Gousseau, P., Blocken, B. and Van Heijst, G.J.F., *CFD simulation of pollutant dispersion around isolated buildings: On the role of convective and turbulent mass fluxes in the prediction accuracy.* Journal of Hazardous Materials, 2011. **194**: p. 422-434.

47 Salim, S.M., Buccolieri, R., Chan, A. and Di Sabatino, S., *Numerical simulation of atmospheric pollutant dispersion in an urban street canyon: Comparison between RANS and LES.* Journal of Wind Engineering and Industrial Aerodynamics, 2011. **99**(2): p. 103-113.

48 Shi, R.F., Cui, G.X., Wang, Z.S., Xu, C.X. and Zhang, Z.S., *Large eddy simulation of wind field and plume dispersion in building array.* Atmospheric Environment, 2008. **42**(6): p. 1083-1097.

49 Lau, G.E. and Ngan, K., *Analysing urban ventilation in building arrays with the age spectrum and mean age of pollutants.* Building and Environment, 2018.

50 Ai, Z.T. and Mak, C.M., *Large-eddy Simulation of flow and dispersion around an isolated building: Analysis of influencing factors.* Computers & Fluids, 2015. **118**(Supplement C): p. 89-100.

51 Spalart, P.R., Jou, W.H., Strelets, M. and Allmaras, S.R., *Comments on the feasibility of LES for wings, and on a hybrid RANS/LES approach.* Advances in DNS/LES, 1997. **1**: p. 4-8.

52 Paik, J., Sotiropoulos, F. and Porté-Agel, F., *Detached eddy simulation of flow around two wall-mounted cubes in tandem.* International Journal of Heat and Fluid Flow, 2009. **30**(2): p. 286-305.

53 Kakosimos, K.E. and Assael, M.J., *Application of Detached Eddy Simulation to neighbourhood scale gases atmospheric dispersion modelling.* Journal of Hazardous Materials, 2013. **261**(Supplement C): p. 653-668.

54 Lateb, M., Masson, C., Stathopoulos, T. and Bédard, C., *Simulation of near-field dispersion of pollutants using detached-eddy simulation.* Computers & Fluids, 2014. **100**(Supplement C): p. 308-320.

55 Liu, J.L. and Niu, J.L., *CFD simulation of the wind environment around an isolated high-rise building: An evaluation of SRANS, LES and DES models.* Building and Environment, 2016. **96**(Supplement C): p. 91-106.

56 Leitl, B. and Schatzmann, M., *Cedval at hamburg university.* URL http://www. mi. uni-hamburg. de/cedval, 2010.

57 Hinze, J., *Turbulence, (1975).* New York, 1959.

58 Smagorinsky, J., *General circulation experiments with the primitive equations: I. The basic experiment.* Monthly weather review, 1963. **91**(3): p. 99-164.

59 Lilly, D.K., *A proposed modification of the Germano subgrid‐scale closure method.* Physics of Fluids A: Fluid Dynamics, 1992. **4**(3): p. 633-635.

60 Spalart, P.R., Deck, S., Shur, M.L., Squires, K.D., Strelets, M.K. and Travin, A., *A New Version of Detached-eddy Simulation, Resistant to Ambiguous Grid Densities.* Theoretical and Computational Fluid Dynamics, 2006. **20**(3): p. 181.

61 Franke, J., *Best practice guideline for the CFD simulation of flows in the urban environment.* 2007: Meteorological Inst.

62 Ai, Z.T. and Mak, C.M., *CFD simulation of flow and dispersion around an isolated building: Effect of inhomogeneous ABL and near-wall treatment.* Atmospheric Environment, 2013. **77**: p. 568-578.

63 Gousseau, P., Blocken, B. and Van Heijst, G.J.F., *Quality assessment of large-eddy simulation of wind flow around a high-rise building: validation and solution verification.* Computers & Fluids, 2013. **79**: p. 120-133.

64 Celik, I.B., Cehreli, Z.N. and Yavuz, I., *Index of resolution quality for large eddy simulations.* Journal of fluids engineering, 2005. **127**(5): p. 949-958.

65 Klein, M., *An attempt to assess the quality of large eddy simulations in the context of implicit filtering.* Flow, Turbulence and Combustion, 2005. **75**(1-4): p. 131-147.

66 Meyers, J., Geurts, B.J. and Baelmans, M., *Database analysis of errors in large-eddy simulation.* Physics of Fluids, 2003. **15**(9): p. 2740-2755.

67 Courant, R., Friedrichs, K. and Lewy, H., *On the partial difference equations of mathematical physics.* IBM journal of Research and Development, 1967. **11**(2): p. 215-234.

68 Gousseau, P., Blocken, B. and Van Heijst, G.J.F., *Large-Eddy Simulation of pollutant dispersion around a cubical building: Analysis of the turbulent mass transport mechanism by unsteady concentration and velocity statistics.* Environmental Pollution, 2012. **167**: p. 47-57.